Title: Cranial suture integrity is maintained by Fgfr3 in zebrafish

Authors : Rachel Pereur [1], Yvan Marc [1], Yuliya Lim [2], Alain Schmitt [3], Marilyne Malbouyres [4], Anatole Chessel [2], Florence Ruggiero [4], Marie-Claire Schanne-Klein [2], Laurence Legeai-Mallet [1] and Emilie Dambroise [1]

Affiliations :

1. Laboratory of Genetics of Developmental Disorders, Imagine Institute, Université de Paris Cité-INSERM UMR1163, Paris, France
2. Laboratory for Optics and Biosciences, Ecole polytechnique, CNRS, INSERM, Institut Polytechnique de Paris, Palaiseau, France
3. Université Paris Cité, CNRS, Inserm, Institut Cochin, F-75014 Paris, France
4. Laboratory of biology and pathology of the matrix, ENS of Lyon, Institut of functional genomics, UMR 5242, Lyon, France

Abstract

Cranial suture formation is a dynamic process requiring precise cellular and molecular coordination to regulate bone growth and suture homeostasis. Despite the recognized role of Fibroblast Growth Factor Receptor 3 (FGFR3) in this process and its association with Muenke syndrome, one of the most common syndromic craniosynostoses, its precise function remains undefined. Through analyses of cranial suture formation and maintenance in a *fgfr3* LoF zebrafish model displaying abnormal suture morphology, we demonstrate for the first time that Fgfr3 plays a pleiotropic role during these events. Transmission electron microscopy and second harmonic generation imaging revealed that Fgfr3 is involved in the proper organization of the collagen network within the suture. By employing specific transgenic reporter lines and studying gene expression of suture mesenchymal stem cell markers via RNAscope in situ hybridization, we show that Fgfr3 is crucial for regulating osteogenesis within the suture. Specifically, Fgfr3 limits the number of osteoprogenitors at the osteogenic front and promotes osteoblast maturation at the suture edge. Finally, our results reveal that Fgfr3-mediated regulation of osteogenesis involves cross-talk between FGF, canonical Wnt, and potentially BMP signaling pathways. In conclusion, these data position Fgfr3 as a central regulator of cranial suture formation and open new perspectives for understanding suture homeostasis and FGFR3-related craniosynostoses.

Introduction

Cranial sutures are essential structures in skull development. Acting as fibrous joints between rigid calvarial bones, they provide plasticity for skull expansion during early brain growth and contribute to skull shape, symmetry, and absorption of mechanical forces through adulthood [1]. In humans, mice, and zebrafish, five primary sutures extend from anterior to posterior, delineating the boundaries between cranial bones: the metopic suture, the two coronal sutures, the sagittal suture, and the lambdoid suture [2]. Their formation is a dynamic process requiring precise cellular and molecular coordination to regulate bone growth and suture homeostasis. At the edges of the approaching bones, an osteogenic front (OF) composed of osteoprogenitor cells is established. These proliferating cells sequentially differentiate into immature and mature osteoblasts forming new bone matrix that is initially restricted to growing bone tips and then at the edges of the suture [3–5]. To support this process, a heterogeneous population of suture mesenchymal stem cells (SuSCs), expressing various markers such as Gli1, Axin2, Prrx1, Ctsk, Bmpr1a, Ddr2, and Grem1a, resides between the OFs, preserving suture patency in a fibrous, unossified state while also contributing to the recruitment of osteoprogenitors at the ossification front. Each subpopulation presents their own properties and participates more or less in the osteogenesis within the OF [5–12]. All these cells are surrounded by an extracellular matrix (ECM) rich in collagens, which provides structural support and participates in the transmission of biomechanical signals, as sutures are subjected to significant tensile and compressive forces, both essential for the regulation of osteogenesis [13–18].

Several signaling pathways and genes involved in suture homeostasis have been implicated in genetic diseases characterized by pathological suture expansion or premature fusion, known as craniosynostosis. This includes Fibroblast Growth Factor Receptor 3 (FGFR3), where both gain-of-function (GoF) and loss-of-function (LoF) mutations lead to distinct cranial suture defects. GoF mutations are associated with syndromic craniosynostosis, as observed in Muenke syndrome, one of the most frequent forms of craniosynostosis, and in Crouzon syndrome with acanthosis nigricans[19,20]. In contrast, LoF mutations result in Camptodactyly-Tall Stature-Scoliosis-Hearing Loss (CATSHL) syndrome, which leads to the formation of ectopic bones along the sutures, known as Wormian bones [21]. However, despite these

findings, *Fgfr3* mouse models with GoF or LoF mutations have failed to fully recapitulate these cranial phenotypes, posing a significant challenge in deciphering the precise role of FGFR3 in cranial suture formation and maintenance [22–24]. Zebrafish, now widely used to study craniofacial development in normal and pathological contexts (including craniosynostoses), has emerged as a relevant model for investigating Fgf signaling and Fgfr3 function during cranial vault formation [5,11,25,26]. Similar to CATSHL syndrome, *fgfr3* LoF zebrafish exhibit microcephaly and Wormian bones [27,28]. Our previous data on a *fgfr3* LoF zebrafish model (*fgfr3*$^{lof/lof}$) demonstrated that *fgfr3* is expressed during cranial bone development, in late-stage osteoprogenitors and both immature and mature osteoblasts, and regulates positively both the expansion and maturation of immature osteoblasts [28]. Interestingly, *fgfr3*$^{lof/lof}$ zebrafish exhibit a dramatic impairment of metopic and sagittal sutures formation, with bones that fail to overlap and remain separated by a thick layer of fibrous tissue. This phenotype, which contrasts with craniosynostosis, makes *fgfr3*$^{lof/lof}$ fish an ideal model for studying the involvement of Fgfr3 in cranial suture homeostasis.

Here, to achieve this goal, we analyzed the key factors involved in the formation and maintenance of cranial sutures in *fgfr3*$^{lof/lof}$ zebrafish, from suture initiation at 12 standard length (SL) to adulthood. We show that the absence of Fgfr3 completely disrupts suture formation, affecting not only the structural integrity of the sutures but also the organization of the collagen network within the sutures and at the bone ends, as shown by transmission electron microscopy (TEM) and second harmonic generation (SHG) microscopy. In addition, using transgenic lines marking osteoprogenitors (Tg: (*runx2;*GFP*)*), and immature (Tg:(*sp7;*mCherry*)*) and mature (Tg: (*bglap;*GFP*)*) osteoblasts, we demonstrate that the absence of Fgfr3 affects the entire membranous ossification process involved in suture formation and maintenance. Finally, by RNAscope *in situ* hybridization of SuSC marker expression, we provide evidence that the absence of Fgfr3 influences osteogenesis through the activation of the canonical Wnt pathway and potentially the BMP pathway.

105 **Results**

106 **Fgfr3 is required for proper cranial suture formation**

107 In adult wild-type zebrafish, metopic, sagittal and coronal sutures (Figure 1A)
108 present the same structure as human coronal sutures, with overlapping bones,
109 osteogenic cells at their edge and a thin layer of SuSCs surrounded by ECM rich in
110 collagens in the middle. We previously reported that *fgfr3*$^{lof/lof}$ metopic and sagittal
111 sutures displayed a failure of bone overlap, with the bones being separated by a thick
112 fibrous tissue at 20 SL [28]. As the metopic suture is among the first to develop in
113 zebrafish, we focused on the role of Fgfr3 during formation of this suture. We used
114 RNAscope *in situ* hybridization to map *fgfr3* expression during metopic suture
115 formation in wild-type fish at three stages: 10 SL (frontal bones approaching), 12 SL
116 (suture formation), and 20 SL (suture maintenance, adult stage) (Figure 1B, C). At 10
117 SL, *fgfr3* was expressed at the OF of the developing cranial bones, and on the forming
118 metopic suture (Figure 1B). At later stages, transversal sections showed *fgfr3*
119 expression within the suture and in osteogenic cells above and below the frontal bones,
120 a region we will refer to as the bone surface (Figure 1C). At 12 SL, we noted that *fgfr3*
121 expression was higher within the suture compared to the bone surface, while at 20 SL,
122 the same level of *fgfr3* expression is observed within the suture and along the bone
123 surface (Figure 1D).

124 To further investigate the progression of the metopic suture in *fgfr3*$^{lof/lof}$ fish over
125 time, we examined it at 12, 20 and 26 SL (Figure 1E). While *fgfr3*$^{+/+}$ fish displayed a
126 well-formed suture at 12 SL, *fgfr3*$^{lof/lof}$ frontal bones remained separated in agreement
127 with our previous data [28]. By 20 and 26 SL, although the bones sometimes came closer
128 together, they still did not overlap in the mutants (Figure 1E). Interestingly, lack of bone
129 overlap was associated with a greater cell number within the *fgfr3*$^{lof/lof}$ metopic suture
130 compared to controls (20 SL: *fgfr3*$^{+/+}$: 28.25 ± 11.82; *fgfr3*$^{lof/lof}$: 49.57 ± 16.95 p=0.0007
131 and 26 SL: *fgfr3*$^{+/+}$: 69.41 ± 19.52; *fgfr3*$^{lof/lof}$: 117.77 ± 64.94 p=0.0060) as well as a
132 greater thickness of *fgfr3*$^{lof/lof}$ bones compared with *fgfr3*$^{+/+}$ bones in adulthood (+129%
133 at 20 SL and +118% at 26 SL in the *fgfr3*$^{lof/lof}$ fish vs *fgfr3*$^{+/+}$ fish) (Figure 1F-G).

134 Interestingly, by performing sagittal sections of *fgfr3*$^{lof/lof}$ heads at 20 SL, we
135 observed that coronal sutures are also affected, suggesting that the absence of Fgfr3
136 impacts all cranial vault sutures in zebrafish similarly (Figure 1 supplement 1A).

137 Increased bone thickness in *fgfr3*$^{lof/lof}$ zebrafish was also observed in the bones forming
138 the coronal suture (+308% at 20 SL and +164% at 26 SL) (Figure 1 supplement 1B).
139 These findings demonstrate that the absence of *fgfr3* disrupts proper cranial
140 suture formation throughout the lifespan of zebrafish and leads to bone expansion,
141 predominantly in thickness rather than length.
142
143 **The absence of Fgfr3 leads to a progressive disruption of Collagen fibrils within**
144 **the suture**
145 Cells within cranial vault sutures of *fgfr3*$^{lof/lof}$ fish are surrounded by a dense ECM
146 rich in collagens, as shown by Sirius red-Alcian blue staining (Figure 2A). In our
147 previous study, we found that the absence of Fgfr3 during cranial vault development
148 leads to the upregulation of the expression of several ECM-regulating genes, including
149 *col6a1*, *col12a1a*, and *col12a1b* [28]. To determine whether this overexpression
150 persisted in sutures, we performed immunofluorescence for ColVI,ColXII, and ColI
151 which is also known to be expressed in cranial sutures. We observed that ColI and
152 ColXII were expressed within the cranial sutures of both *fgfr3*$^{+/+}$ and *fgfr3*$^{lof/lof}$ fish at 12
153 SL, and that the expression levels of both proteins are increased only in older *fgfr3*$^{lof/lof}$
154 fish (20 SL) (Figure 2B-C). In contrast, ColVI was expressed to a lesser extent at both
155 stages and genotypes (Figure 2D). As ColXII is known to interact with ColI fibrils and
156 to regulate collagen fibril spacing and assembly during fibrillogenesis, we further
157 analyzed collagen fibrils within the metopic suture by TEM at 9, 12 and 20 SL (Figure
158 2E) [29]. At 9 SL, metopic sutures were not formed, and collagen fibrils were poorly
159 organized for both genotypes. By 12 SL, metopic sutures in controls were formed with
160 organized fibril clusters, while in mutants, where frontal bones remained separated,
161 fibrils remained disorganized, similar to 9 SL. At 20 SL, fibrils in *fgfr3*$^{lof/lof}$ fish were
162 clustered, similar to controls, but appeared less organized, with the size of each fibril
163 appearing more heterogeneous (Figure 2E). This observation was confirmed by
164 measurement of the transverse area of each fibril (Figure 2F). In controls, fibril size
165 progressively increased over time, with most fibril areas not exceeding 1000 nm² at 20
166 SL. In *fgfr3*$^{lof/lof}$ zebrafish, we first observed no change in fibril size between 9 and 12
167 SL, consistent with the delay in frontal bone closure. Then, at 20 SL, significant
168 heterogeneity in fibril size was observed, with larger fibrils emerging, exceeding 2500
169 nm². This increase was further confirmed by the larger average collagen fibril area for
170 *fgfr3*$^{lof/lof}$ at 20 SL compared to controls (*fgfr3*$^{+/+}$: 794.5 ±123.1 nm²; *fgfr3*$^{lof/lof}$: 945.1

171 ±146.1nm²; p=0.05), showing an impairment of fibrillogenesis in adulthood within the
172 suture in the mutants (Figure 2G).
173 Noting defects in collagen fibrils at the suture, and bone thickening near sutures,
174 we examined whether collagen fibers in the frontal bones were also affected by the
175 absence of Fgfr3 over time. We performed polarization-resolved SHG microscopy at
176 12 and 26 SL to study collagen fibers structure and organization, assessing the signal
177 intensity and the circular standard deviation of the collagen orientation distribution in a
178 region close to the suture (zone 1) and another farther away (zone 2) (Figure 3A). The
179 circular standard deviation of the collagen orientation distribution measures the degree
180 of variability in the orientation of collagen fibers, providing insight into their alignment
181 and organization at the scale of the image. By 12 SL, no defects in either the structure
182 or the organization were observed in collagen fibers in both regions (Figure 3B and C).
183 In contrast, by 26 SL, although no defect in the collagen structure was noted, a
184 significant disorganization of collagen fibers was observed only in the region adjacent
185 to the suture (zone1) (26 SL *fgfr3*$^{+/+}$: 24.96 ± 4.39 degrees; *fgfr3*$^{lof/lof}$: 31.62 ± 4.13
186 degrees; p=0.028) (Figure 3B and D). The absence of structural defects and the
187 progressive, localized disorganization of bone collagen fibers at the bone ends suggest
188 that this defect is not directly due to the absence of Fgfr3 but may instead be secondary
189 to changes in suture shape.
190
191 **The absence of Fgfr3 results in the excessive expansion of osteoprogenitors**
192 **and inhibits the maturation of osteoblasts at the suture edge**
193 To rule out the hypothesis that excessive bone resorption at the suture edge
194 could be responsible for the change in the shape of the suture, we first assessed
195 osteoclast activity using tartrate-resistant acid phosphatase (TRAP) staining at 12, 20
196 and 26 SL. No TRAP positive cells were observed in the suture of either *fgfr3*$^{+/+}$ or
197 *fgfr3*$^{lof/lof}$ fish at the stages tested (Figure 4 supplement 1). This confirmed previous
198 data indicating that osteoclasts are not involved in suture homeostasis in zebrafish,
199 and rules out the possibility that the suture abnormalities observed in our model result
200 from increased osteoclast activity [30]. We then further explored osteogenesis at the
201 metopic suture from 12 SL to adulthood in *Tg(runx2:GFP; fgfr3*$^{lof/lof\ or\ +/+}$*)* and
202 *Tg(sp7:*mCherry*; bglap:*GFP*; fgfr3*$^{lof/lof\ or\ +/+}$*)* lines. Regarding osteoprogenitors, at 12
203 SL, *runx2*:GFP+ cells in *fgfr3*$^{+/+}$ fish were localized only at the tips of the formed bones,
204 known as the OF. In contrast, in *fgfr3*$^{lof/lof}$ fish, *runx2:*GFP+ cells were not only

205 distributed at the tips of the bones but also along the bone surface (Figure 4A). At 20
206 SL, whereas *runx2*:GFP+ cells in *fgfr3*$^{+/+}$ fish were still present only at the tip of the
207 bones, *runx2*:GFP+ cells in *fgfr3*$^{lof/lof}$ fish were distributed along the entire edge of the
208 sutures and are no longer present on the bone surface (Figure 4A). This was confirmed
209 by the increased percentage of *runx2*:GFP+ cells present at the edge of the *fgfr3*$^{lof/lof}$
210 sutures compared to controls (*fgfr3*$^{+/+}$: 44.9 ± 24.4% ; *fgfr3*$^{lof/lof}$: 72.1 ±12.5% ; p=0.04)
211 (Figure 4C). Given that osteoprogenitors are characterized by a round shape, we
212 analyzed nuclear circularity of cells present along the suture (Figure 4 supplement 2A-
213 D). For the control, we separately analyzed the nuclei of cells at the OF and those at
214 the edge of the sutures. As expected, in *fgfr3*$^{+/+}$ fish, OF nuclei were significantly more
215 circular than those along the suture (Figure 4 supplement 2D). In *fgfr3*$^{lof/lof}$ fish, the
216 nuclei along the suture resembled the circularity of OF nuclei in *fgfr3*$^{+/+}$ fish (Figure 4
217 supplement 2D). The modification of shape nuclei was not observed along the bone
218 surface (Figure 4 supplement 2B). These findings were further confirmed by TEM
219 (Figure 4 supplement 2C) and suggests the presence of extra progenitors (*runx2*
220 positive cells) along the suture of *fgfr3*$^{lof/lof}$ fish.

221 Next, we studied the impact of the absence of Fgfr3 on immature (*sp7-positive*)
222 and mature (*bglap-positive*) osteoblasts. In both *fgfr3*$^{+/+}$ and *fgfr3*$^{lof/lof}$ fish, immature
223 osteoblasts were present throughout the bone surface and along the suture at all
224 stages (Figure 4B and Figure 4 supplement 3A). The quantification of immature
225 osteoblasts at 20 and 26 SL showed significantly more immature osteoblasts at the
226 edge of the metopic suture in the *fgfr3*$^{lof/lof}$ model compared to controls, with no
227 difference along the bone surface (suture, *fgfr3*$^{+/+}$: 34.3 ± 14.3%; *fgfr3*$^{lof/lof}$: 74.1 ±
228 11.7%; p<0.0001; bone surface, *fgfr3*$^{+/+}$: 46.7 ± 6.3%; *fgfr3*$^{lof/lof}$: 38.0 ±5.9%; p=0.315)
229 (Figure 4D and Figure 4 supplement 3B). Regarding mature osteoblasts, in *fgfr3*$^{+/+}$ fish
230 we observed their presence throughout the bone surface and along the suture at all
231 stages (Figure 4E and Figure 4 supplement 3C). Interestingly, in *fgfr3*$^{lof/lof}$, while mature
232 osteoblasts were present throughout the bone surface similar to controls, there was a
233 near absence of mature osteoblasts within the suture at all stages (suture, *fgfr3*$^{+/+}$: 29.4
234 ± 10%; *fgfr3*$^{lof/lof}$: 1.9 ± 2.4%; p<0.0001; bone surface, *fgfr3*$^{+/+}$: 52.7 ± 8.1%; *fgfr3*$^{lof/lof}$:
235 43.7 ± 9.8%; p=0.1586). To determine whether these events occur in other sutures,
236 we analyzed immature and mature osteoblasts in the coronal suture at 26 SL(Figure 4
237 Supplement 3D-F). In *fgfr3*$^{lof/lof}$ coronal sutures, a higher number of immature
238 osteoblasts (*fgfr3*$^{+/+}$: 46.2 ± 6.6%; *fgfr3*$^{lof/lof}$: 75.3 ± 5.9%; p=0.0011) and an absence of

239 mature osteoblasts (*fgfr3*$^{+/+}$: 50.9 ± 20.6%; *fgfr3*$^{lof/lof}$: 0 ± 0%; p<0.0001) were found
240 compared to controls, with no significant difference for the immature and mature
241 osteoblasts along the bone surface (*sp7*: 26 SL, *fgfr3*$^{+/+}$: 60.8% ± 17.8%; *fgfr3*$^{lof/lof}$:
242 73.9% ± 7.5%; p=0.1355; *bglap*: 26 SL, *fgfr3*$^{+/+}$: 47.8% ± 17.6%; *fgfr3*$^{lof/lof}$: 34.6% ±
243 7.6%; p=0.3450). We conclude that the same osteoblast maturation abnormalities are
244 present in *fgfr3*$^{lof/lof}$ coronal sutures as in the metopic suture.
245 To better understand the higher number of *runx2* and *sp7* positive cells as well
246 the absence of *bglap* positive cells within the suture of the *fgfr3*$^{lof/lof}$ fish, we first studied
247 cell proliferation rates at 12 and 20 SL by performing balneation EdU experiments.
248 Surprisingly, we found no difference at either stage (Figure 4F, H) suggesting that the
249 absence of Fgfr3 does not lead to a proliferation defect of osteoprogenitors and
250 immature osteoblasts within the suture. Subsequently, we investigated apoptosis by
251 performing a TUNEL assay. At 12 SL, we observed no apoptosis for either genotype.
252 However, at 20 and 26 SL, a few randomly localized apoptotic events were observed
253 only within the *fgfr3*$^{lof/lof}$ suture (20 SL; *fgfr3*$^{+/+}$: 0.7%; *fgfr3*$^{lof/lof}$: 5.2%; p=0.0294; 26 SL;
254 *fgfr3*$^{+/+}$: 0.6%; *fgfr3*$^{lof/lof}$: 8.7%; p=0.0019) (Figure 4G, I). Since apoptosis appears to
255 occur randomly and later than the observed absence of mature osteoblasts, it does not
256 account for their disappearance. The latter is likely due to the inhibition of maturation
257 of immature osteoblasts.
258
259 All these data demonstrate that the absence of Fgfr3 seems to have a dual effect
260 specifically within the cranial sutures. On one hand, it induces the expansion of
261 osteoprogenitors (which normally localize only to the tip of the bones) all along the
262 suture edge, which then differentiate into immature osteoblasts. On the other hand, it
263 inhibits immature osteoblasts maturation, leading to their accumulation at the suture
264 edge.
265
266 **The absence of Fgfr3 alters the SuSC marker profile, highlighting the**
267 **downregulation of the BMP antagonist Grem1 and the activation of the Wnt**
268 **signaling pathway within the suture.**
269 Given the greater number of osteoprogenitors in the *fgfr3*$^{lof/lof}$ sutures compared
270 to the control (Figure 4D), we also studied the expression of *prrx1, gli1, axin2,* and
271 *grem1* at 12 and 20 SL. All these genes are known to be expressed in distinct
272 populations of SuSCs, and play a crucial role in maintaining suture patency (Figure

273 5A-B) [11,31,5]. *prrx1* was expressed within the suture and bone surface at both stages,
274 with no difference in expression between the genotypes (Figure 5A-B). The expression
275 of *gli1* was nearly absent at 12 and 20 SL in *fgfr3*$^{+/+}$ sutures, and at 20 SL in *fgfr3*$^{lof/lof}$
276 sutures. We only observed a slightly higher expression of *gli1* at 12 SL in *fgfr3*$^{lof/lof}$
277 sutures compared to controls (Figure 5A-B), but this is unlikely to explain the increased
278 number of cells within the suture and may instead reflect only the delay of the mutant
279 cranial vault growth.

280 The expression of *grem1,* which encodes Gremlin1, an antagonist of BMP, was
281 restricted to the suture and increased from 12 to 20 SL in controls. In contrast, in
282 *fgfr3*$^{lof/lof}$*,* its expression at 12 SL was restricted to the tips of the bones, and was
283 significantly lower at 20 SL compared to controls (20 SL: *fgfr3*$^{+/+}$: 2.3 ±1.2
284 transcripts/nucleus (t/n); *fgfr3*$^{lof/lof}$: 0.5± 0.3 t/n; p=0.0001) (Figure 5A-B).

285 However, we observed a significant upregulation of *axin2* in mutants compared
286 to controls at 12 SL within the suture, which appeared to be maintained over time,
287 although not significantly (12 SL: *fgfr3*$^{+/+}$: 0.3 ±0.1 t/n; *fgfr3*$^{lof/lof}$: 0.8± 0.2 t/n; p=0.0017;
288 20 SL: *fgfr3*$^{+/+}$: 0.4 ±0.3 t/n; *fgfr3*$^{lof/lof}$: 0.6± 0.2 t/n; p=0.09). Given that *axin2* seemed to
289 be more expressed at the edges of the suture, where osteoprogenitors and immature
290 osteoblasts are localized, we analysed its expression specifically at the suture edge
291 (Figure 5C). We found higher expression of *axin2* at both 12 and 20 SL in *fgfr3*$^{lof/lof}$
292 suture edges compared to controls (12 SL: *fgfr3*$^{+/+}$: 0.3 ±0.1 t/n; *fgfr3*$^{lof/lof}$: 0.7± 0.2 t/n;
293 p=0.004; 20 SL: *fgfr3*$^{+/+}$: 0.4 ±0.2 t/n; *fgfr3*$^{lof/lof}$: 0.7± 0.1 t/n; p=0.03). As Axin2 is both
294 a Wnt/β-catenin target gene and a negative regulator of the Wnt canonical pathway,
295 we aimed to determine whether there is abnormal activation of the Wnt signaling
296 pathway at the edge of *fgfr3*$^{lof/lof}$ metopic sutures [32]. To do this, we used the Wnt
297 reporter line *Tg(7xTCF-Xla.Siam:GFP)ia4* to generate *Tg(7xTCF-Xla.Siam:GFP)*^{ia4}*;*
298 *fgfr3*$^{lof/lof\ or\ +/+}$ fish and examined the presence of GFP-positive cells at the metopic
299 suture at 12 SL. We observed that GFP positive cells were localized at the tips of the
300 frontal bones in both genotypes but a greater number of positive cells were present in
301 *fgfr3*$^{lof/lof}$ fish compared to controls, indicating activation of the Wnt pathway (*fgfr3*$^{+/+}$:
302 0.6 ±0.6; *fgfr3*$^{lof/lof}$: 5.1± 1.1; p<0.0001) (Figure 5D and E).

303 The interplay between FGF and Wnt signaling in cranial sutures was recently
304 highlighted by Bobzin et al., who showed in a FGFR2 LoF mouse model that FGF
305 signaling regulates anterior fontanelle closure in mice by inhibiting Wnt signaling,
306 guiding Scx- and Tnmd-expressing ectocranial mesenchyme toward bone and

307 cartilage differentiation [33]. Interestingly, *tnmd* expression was found downregulated in
308 *fgfr3* LoF zebrafish during cranial bone development [28]. Therefore, we investigated
309 whether Fgfr3 LoF and Wnt pathway activation influenced the expression of *tnmd* or
310 *scx* within the suture at 20 SL. Contrary to findings in mice, neither gene was
311 dysregulated nor restricted to a specific cell population in either the control or *fgfr3*$^{lof/lof}$
312 suture (Figure 5 supplement 1). These findings suggest that the mechanisms leading
313 to suture anomalies differ between the animal models. Nevertheless, our data indicate
314 that the absence of Fgfr3 induces overactivation of Wnt signaling at the suture edge
315 and potentially of the BMP pathway within the suture.
316

317 **The absence of Fgfr3 is not compensated by other Fgfrs and leads to the**
318 **overexpression of Fgf18 within the suture**

319 Our data reveal that Fgfr3 has a localized effect within the suture, which
320 becomes particularly evident in adulthood (from 20 SL) with the presence of ectopic
321 osteoprogenitors and the absence of mature osteoblasts exclusively at the suture
322 edges, while osteogenesis along the bone surface appears unaffected. These results
323 were unexpected, as *fgfr3* expression was observed both within the sutures and along
324 the bone surface (Figure 1B and C). This differential activity of Fgfr3 may reflect the
325 varying expression levels of its ligands, such as Fgf2 and Fgf18, which are known to
326 be expressed during zebrafish cranial vault development [28]. Therefore, we examined
327 the expression of *fgf2* and *fgf18* (Figure 6A). With regard to *fgf2*, no differential
328 expression was observed between the bone surface and the suture, regardless of the
329 genotype at 12 and 20 SL (Figure 6B and C)**.** However, in the case of *fgf18*, although
330 its expression was low in both the bone surface and suture in *fgfr3*$^{+/+}$ fish, we observed
331 higher expression of *fgf18* in *fgfr3*$^{lof/lof}$ sutures compared to the *fgfr3*$^{+/+}$ sutures at both
332 stages (12SL: *fgfr3*$^{+/+}$: 0.3 ±0.1 t/n; *fgfr3*$^{lof/lof}$: 0.7± 0.2 t/n; p=0.004; 20 SL: *fgfr3*$^{+/+}$: 0.4
333 ±0.2 t/n; *fgfr3*$^{lof/lof}$: 0.7± 0.1 t/n; p=0.03) (Figure 6B and C). The absence of differential
334 expression of *fgf2* and *fgf18* between the bone surface and suture in *fgfr3*$^{+/+}$ fish may
335 suggest that the localized role of Fgfr3 within the suture is not dependent on the
336 expression of these two ligands. However, these results highlight that the absence of
337 Fgfr3 leads to an increase of *fgf18* expression specifically within the suture.

338 We next examined the expression of *fgfr1a*, *fgfr1b* and *fgfr2* (Figure 6D-G).
339 *fgfr1b* was consistently expressed at a low level throughout cranial suture formation,
340 with no significant variation observed based on its spatial distribution or genotype. The

341 expression of *fgfr1a* and *fgfr2* also did not differ between control and mutant. But when
342 we compared Fgfr2 expression in suture vs bone surface, we observed that *fgfr2* is
343 significantly more expressed in both the *fgfr3*$^{+/+}$ and *fgfr3*$^{lof/lof}$ bone surface at 20 SL
344 (*fgfr3*$^{+/+.}$ bone surface: 1.5 ±0.5 t/n; suture: 0.8± 0.4 t/n; p=0.004; *fgfr3*$^{lof/lof}$; bone
345 surface: 1.5 ±0.4 t/n; suture: 0.6± 0.2 t/n; p<0,0001) suggesting a more prominent role
346 for *fgfr2* in the bone surface (Figure 6 supplement 1). These results revealed, first, that
347 neither the absence of Fgfr3 nor the increased expression of Fgf18 leads to an
348 increase in expression of other Fgfrs; second, that other Fgfrs may play a more
349 prominent role than Fgfr3 at the bone surface; and third, the key role of Fgfr3 for proper
350 suture formation in zebrafish.
351

352 **Discussion**

353 By examining cranial sutures from initiation to adulthood in our LoF Fgfr3 zebrafish
354 model, we demonstrated for the first time that Fgfr3 is essential for the proper formation
355 of cranial sutures (Figure 7) [28]. We showed that the absence of bone overlap in *fgfr3*$^{lof/lof}$
356 cranial sutures was linked to an increased number of cells surrounded by an ECM, with
357 defects in collagen fibrilllogenesis. In addition, we observed a progressive bone
358 thickening accompanied by disorganization of collagen fibers at their tips. Furthermore,
359 we provide evidence that Fgfr3 is crucial for limiting the number of osteoprogenitors at
360 the bone ends and for promoting the maturation of osteoblasts specifically at the suture
361 edge. Finally, our results suggest that Fgfr3 regulation of cranial suture formation
362 involves both the canonical Wnt and BMP signaling pathways and highlight a potential
363 regulatory loop through the modulation of *fgf18* expression. These results are essential
364 as until now, the involvement of FGFR3 in cranial suture formation had only been
365 illustrated by the existence of the craniosynostoses associated with FGFR3 mutations
366 (Muenke and CAN syndrome) and a few studies reporting occasional premature fusion
367 of coronal sutures in mouse models expressing Fgfr3 GoF mutations [19,20,23,34].
368

369 Our study focuses on the late stages of cranial vault development, when the bones
370 converge and the suture forms. In this phase, periosteal osteoblasts drive skull
371 widening and remodeling, while suture osteoblasts are responsible for maintaining
372 continuous cranial expansion and keeping the suture open. Analysis of osteogenesis
373 at both sites using *Tg(runx2:GFP; fgfr3*$^{lof/lof\ or\ +/+}$*),* and *Tg(sp7:*mCherry*; bglap:*GFP*;*

374 *fgfr3*$^{lof/lof\ or\ +/+}$) lines showed that Fgfr3 loss does not affect osteogenesis along the bone
375 surface. In contrast, from the suture initiation onwards, at bone extremities, Fgfr3
376 absence increases the number of osteoprogenitors (Runx2-positive cells), which are
377 no longer confined to bone tips, leading to an expanded ossification front over time.
378 Interestingly, this increase of Runx2 positive cells associated with the lack of bone
379 overlap has been described in *sp7*$^{-/-}$ fish [35]. In that study, the authors linked the
380 increase in Runx2 positive cells to the absence of *sp7* expression, which is essential
381 for the normal progression of osteoblast differentiation. In contrast, in *fgfr3*$^{lof/lof}$ fish,
382 differentiation appears blocked not at the transition from osteoprogenitors to immature
383 osteoblasts but from immature to mature osteoblasts. This is evidenced by the higher
384 number of *sp7*$^{+}$ cells and the absence of *bglap*$^{+}$ cells at the suture edge, unrelated to
385 apoptosis. These findings showed that Fgfr3 positively regulates osteoblast maturation
386 during suture formation, as we demonstrated at an earlier stage of cranial bone
387 development [28]. However, the increase in *runx2*- and *sp7*-positive cells remains
388 complex to interpret, as no increase in osteoprogenitor or immature osteoblast
389 proliferation was detected at the suture edge. Instead, it may result from enhanced
390 recruitment of osteoprogenitors from differentiating SuSCs and/or the accumulation of
391 cells that fail to mature. In any case, this osteogenesis defect, localized at bone
392 extremities but not along the bone surface, likely underlies both the progressive
393 widening of the bone extremities and a part of the increased cellularity observed within
394 the suture.
395
396 Our work reveals that the absence of Fgfr3 leads to changes in the expression of
397 *grem1* and *axin2*, which are both known to be expressed in SuSCs and are involved
398 respectively, in the BMP and canonical Wnt signaling pathways, two major pathways
399 crucial for cranial suture homeostasis and osteoblast differentiation [36]. First, we
400 observed a significant decrease in *grem1* expression within the sutures in the absence
401 of Fgfr3. Grem1 is an antagonist of the BMP signaling pathway recently identified as a
402 marker of a SuSC subpopulation in zebrafish [5]. Interestingly, Farmer et al., reported
403 that the absence of *grem1* in zebrafish leads to a slight delay of cranial vault formation.
404 However, when Grem1 is absent along with Nog2 and Nog3, two other BMP
405 antagonists, it leads to overactivation of BMP signaling in the suture, resulting in the
406 same suture anomalies seen in our *fgfr3*$^{lof/lof}$ model (e.g., failure of bone overlaps and
407 the presence of ectopic bone). This phenotypic similarity and the decreased *grem1*

408 expression in *fgfr3*$^{lof/lof}$ metopic sutures suggest that the absence of Fgfr3 may increase
409 BMP signaling within the suture. Notably, BMP pathway activation was also reported
410 in the *sp7*$^{-/-}$ zebrafish model further supporting our hypothesis [35]. As the BMP pathway
411 promotes osteogenesis, its activation in the absence of Fgfr3 may increase
412 osteoprogenitor recruitment along the suture. Further experiments are required to
413 validate this hypothesis and to determinate the link between the absence of Fgfr3 and
414 the decrease of *grem1* expression. Furthermore, existing data on cranial sutures
415 suggest the opposite that FGF signaling promotes BMP signaling [37,38]. Additionally, it
416 was reported in mouse model that FGF18 modulates *Grem1* expression via the
417 activation of FGFR3 in chondrocytes located in synchondroses or in articular cartilage
418 [39,40]. Interestingly we noted in absence of Fgfr3 an overexpression of *fgf18*, one of the
419 Fgfr3 ligands essential for cranial vault development[41]. Although regulation of Grem1
420 by Fgf18 in cranial sutures has not been documented, we could hypothesize that Fgf18
421 regulates *grem1* expression through its binding to other Fgfrs. At the RNA level, we did
422 not observe an increase in *fgfr1a*, *fgfr1b*, and *fgfr2* expression within the suture in the
423 absence of Fgfr3, suggesting the absence of a compensatory mechanism.
424 Nevertheless, since *fgfr1a, fgfr1b, and fgfr2* are expressed within the suture, albeit to
425 a lesser degree than Fgfr3, their activation through Fgf18 binding remains a possibility.
426
427 Additionally, we showed that the absence of Fgfr3 appears to lead to overactivation
428 of the Wnt signaling pathway at the suture edges, as evidenced by both the
429 overexpression of *axin2*, a Wnt/β-catenin target gene and the increased number of
430 *7xTCF-Xla.Siam:*GFP-positive cells in Fgfr3 deficient fish. This suggests that Fgfr3
431 may act as a potential inhibitor of the canonical Wnt signaling pathway. Notably, Fgfr3
432 has already been described as such during chondrogenesis, specifically in pharyngeal
433 skeleton formation in zebrafish [27]. Moreover, recent work by Bobzin et al. highlighted
434 crosstalk between FGF and Wnt/β-catenin pathways in sutures of mice, demonstrating
435 that FGFR2 activation at the OF of the frontal bones regulates anterior fontanel closure
436 by inhibiting Wnt signaling through Wif1 [33]. Within the suture, Wnt signaling is involved
437 in regulating the number of SuSCs and also osteoblast differentiation [42]. Aberrant β-
438 catenin activation has been shown to widen all cranial sutures in mice, accompanied
439 by increased *Runx2* and *Sp7* expression, the absence of the mature osteoblast marker
440 *Osteopontin*, and enhanced BMP signaling [43]. These findings align with our

observations and further support that Fgfr3 might promote maturation of osteoblasts via the inhibition of canonical Wnt signaling in cranial sutures.

Notably, *Fgf18* is a direct Wnt target gene, regulated positively via a TCF/Lef binding site, in cooperation with RUNX2 [44]. Thus, Wnt pathway activation may drive *fgf18* overexpression in the absence of Fgfr3, thereby outlining the framework of the interplay between the Fgfr3, Wnt, and BMP pathways.

Finally, our work provides evidence that the absence of Fgfr3 may impact osteogenesis not only through direct pathway activation but also by altering the microenvironment of the cells, particularly the collagen network, which, by transmitting biomechanical signals influences cell fate. In our previous study, we showed that Fgfr3 loss leads to the overexpression of ECM-regulating proteins like *col6a1, col12a1a,* and *col12a1b* (Dambroise et al., 2020). Collagen XII is a FACIT collagen known to bind to collagen I fibrils, contributing to the collagen suprastructure and helping to absorb biomechanical stress [45]. We show here that the loss of Fgfr3 disrupts the organization of ColI fibrils in the bones near the suture and within the suture itself, due to both a delay in cranial suture formation and a modification of its shape. This is accompanied by a fibrillogenesis defect, potentially linked to ColXII overexpression, as ColXII regulates both collagen maturation and organization [15,46]. We suggest that modifications in the osteogenic cell environment, including collagen network remodeling and the predominance of lateral over longitudinal bone growth, may alter the mechanical forces exerted on osteogenic cells within the suture. These changes could influence cell fate and potentially explain the progressive emergence of random apoptosis, an as-yet unexplained phenomenon.

In conclusion, our work using a zebrafish model is the first to demonstrate that Fgfr3 is a crucial regulator of cranial suture formation, essential for proper osteogenesis and suture development (Figure 7). We highlight its importance in the regulation of BMP and Wnt pathways within the sutures, the underlying mechanisms of which remain to be validated and further explored. Altogether, these findings open new perspectives for understanding suture homeostasis and FGFR3-related craniosynostoses, paving the way for new targeted therapies.

474 **Materials and methods**

475 ***Zebrafish husbandry, fgfr3^{lof} fish and transgenic lines***

476 Zebrafish were raised, hatched and maintained in an aquatic facility at 28°C (approval
477 number 2018080216094268 and APAFIS #36172-2022041412092374 v1), in
478 accordance with European Directive 2010/63/EU for animals. Developmental stages
479 were determined by the standard length (SL) of the fish, measured from the snout to
480 the caudal peduncle [47]. *fgfr3^{lof}* fish correspond to the *fgfr3^{lof1}* line described previously
481 [28]. Transgenic lines *Tg(runX2 :GFP), Tg(sp7:mCherry), Tg(bglap:GFP)* [48] and
482 *Tg(7xTCF-Xla.Siam:GFP)^{ia4}* [49] labelling respectively osteoprogenitors, immature
483 osteoblasts, mature osteoblasts and activation of Wnt signalling have been previously
484 described.

485

486 ***Genotyping***

487 Genomic DNA was isolated from caudal fin biopsies under anaesthetic with
488 benzocaine (100mg/L). Tissues were lysed in 10 mM Tris-HCl, pH 8.5, 2 mM EDTA,
489 pH 8, 0.2% Triton X-100, and 250 µg/mL proteinase K (Sigma-Aldrich, St. Louis, MO,
490 USA) for at least 1 hr at 55°C. The samples were genotyped in heteroduplex mobility
491 assay using the following primers *fgfr3lof*_F: 5'- TGAACGATCCCAGGAATCCC -3'
492 and *fgfr3lof*_R: 5'- GGTGAGAATGAAGAGCACGC -3'.

493

494 ***Histological analyses***

495 Zebrafish at 12, 20 and 26 SL were fixed for 24 hrs in 4% paraformaldehyde at 4°C,
496 the heads were decalcified in a 0.5M EDTA solution pH8 for 1 to 5 days, then
497 embedded in paraffin. Paraformaldehyde-Fixed and Paraffin-Embedded (FFPE) (4µm)
498 sections were cut either transversally or sagittally. Haematoxylin Eosin (HE) and Sirius
499 red-Alcian blue staining were performed after dewaxing with Xylene substitute, Neo-
500 Clear® followed by rehydration with decreasing ethanol baths. For HE staining, the
501 sections were incubated sequentially with Haematoxylin for 30 seconds, $LiCO_3$ for 2
502 seconds and Eosin for 10 seconds. For Sirius Red-Alcian blue staining, sections were
503 incubated in Weigert's solution (Hematein 0.1g/mL in EtOH 95° and FeCl3 29% HCl
504 37% v/v) for 5 minutes, washed with acetic acid 1%, incubated 30 min with Alcian blue
505 (1mg/mL; 10% HCl 1N), and finally treated with 0.1% direct red diluted in aqueous
506 saturated picric acid for 2 hours. Image acquisitions were performed using an Olympus

507 IX81 microscope equipped with an Olympus IX2-UCB camera. For HE staining, the
508 sample sizes were n=6 *fgfr3*$^{+/+}$ and n=6 *fgfr3*$^{lof/lof}$ at 12SL, n=6 *fgfr3*$^{+/+}$ and n=8 *fgfr3*$^{lof/lof}$
509 at 20SL and n=10 *fgfr3*$^{+/+}$ and n=9 *fgfr3*$^{lof/lof}$ at 26SL. Quantification of bone thickness
510 was performed on the two bones of one section per individual using the Fiji software
511 (ImageJ). For Sirius Red-Alcian blue, n=6 *fgfr3*$^{+/+}$ and n=6 *fgfr3*$^{lof/lof}$ at each stage were
512 analyzed.
513
514 ***Immunohistochemistry (IHC)***
515 Zebrafish at 12 SL, 20 SL and 26 SL were fixed for 24 hrs in 4% paraformaldehyde at
516 4°C, heads were decalcified for 1 to 5 days in a 0.5M EDTA solution pH8 and
517 impregnated in sucrose 30% during at least 10 days, then, embedded in frozen
518 medium containing 30% sucrose and 7% gelatine. 20 µm sections were cut in
519 transverse orientations. The polyclonal primary antibodies used are anti-Collagen I
520 (Col1α1, Abcam, ab23730), anti-collagen α1 VI (Col6a1, [50]), anti-zebrafish collagen
521 XII antibodies (Col12a1, [51]), anti-mCherry (Takara, 632496) and anti-GFP (Invitrogen;
522 A11122). Initial steps of IHC and blocking buffers depended on the primary antibody
523 used. For ColI labelling, after six 10-minutes washes with PBSTr (Phosphate-Buffered
524 Saline (PBS (Gibco)) Triton-X100 0,5%), the sections were blocked in blocking buffer
525 BB1 (BSA 4%; Triton-X100 0.1%, PBS) for 1hr at room temperature (RT) and then
526 incubated overnight at 4°C with anti-ColI diluted 1:200 in BB1. Before secondary
527 antibody incubations, sections were washed three times for 5 min. For ColXII, mCherry
528 and GFP labelling, the sections were incubated at RT for 1 hr in BB2 (3% sheep serum;
529 1% BSA in PBS), followed by a 1 hr incubation with the corresponding primary antibody
530 diluted 1:250 in BB2 and then washed three times for 5 min with PBS. For Col6
531 labelling, after 20 min wash in PBS, sections were blocked in BB3 (Goat serum 5%
532 diluted in PBS) for 30 min, incubated overnight at 4°C with the corresponding primary
533 antibody diluted 1:400 in BB3 and washed three times for 5 min with PBS. The final
534 steps of IHC for whole labelling consist of a 1 hr incubation with an Alexa fluor™ goat
535 anti-rabbit 594 or 647 (Invitrogen) diluted 1:500 in PBS followed by three 5-minutes
536 washes with PBS and mounting of the slides in DAPI Fluoromount-G ™ (Electron
537 Microscopy Sciences - #17984-24). IHC were imaged with a Spinning Disk Zeiss
538 controlled by Zen Blue software (Olympus, Tokyo, Japan) and processed on the Fiji
539 software (ImageJ) to combine all the images into one containing the maximum intensity
540 information for each pixel. The analysis of ColI, ColVI and ColXII, which are not

541 quantitative was assessed at least on n=3 per genotype for each different stage. The
542 mCherry and GFP labelling for the *Tg(runx2 :GFP), Tg(sp7:mCherry), Tg(bglap:GFP)*
543 were quantified for each stage with at least n=5 samples on one section from each
544 individual at 20 and 26 SL per genotype. The quantification represents the ratio
545 between the number of positively labeled cells and the number of DAPI-stained cells.
546

547 ***EdU and TUNEL labelling***

548 For EdU analyses, 12 and 20 SL*Tg(runX2 :GFP)* fish were immersed in an EdU
549 solution at 12.5 µg/ml during 48hpf. EdU incorporation was subsequently detected on
550 frozen sections (30% sucrose, 7% gelatin) for 12 SL fish and on FFPE sections for 20
551 SL fish. The EdU was detected using the EdU Click-iT Plus EdU Alexa Fluor 647
552 Imagin g kit (Life Technologies, Carlsbad, CA, USA), following the manufacturer's
553 protocol. Sample sizes were n=6 $fgfr3^{+/+}$ and n=6 $fgfr3^{lof/lof}$ at each stage. TUNEL assay
554 were performed on the FFPE sections using the DeadEnd Fluorometric TUNEL system
555 (Promega, Madison, WI, USA), following the manufacturer's instructions
556 (permeabilization step with proteinase K at 10mg/mL diluted in a PBS at 1:500 for 7
557 min). Images were captured with a Spinning Disk Zeiss controlled by Zen Blue software
558 (Olympus, Tokyo, Japan) and processed using the Fiji software (ImageJ) to combine
559 all images into one containing the maximum intensity information for each pixel. The
560 TUNEL experiment was quantified at 20SL and 26SL for n=8 per genotype on two
561 adjacent sections per individual. At 12SL, TUNEL experiment was performed only on
562 n=3 per genotype due to the absence of positive cells.
563

564 ***RNAscope Assay***

565 RNAscope Assays were performed on FFPE sections according to the manufacturer's
566 instructions « RNAscope Multiplex Fluorescent Reagent Kit v2 Assay » provided by
567 ACD a bio-techne brand. After dewaxing, the slides were incubated with Target
568 Retrieval and Protease Plus reagents for 15 minutes and 30 minutes, respectively. The
569 zebrafish *fgfr1a* (C1-409441); *fgfr1b* (C2-409451); *fgfr2* (C1-420961); *fgfr3* (C1-
570 438971); *fgf2* (C1-420951); *fgf8a* (C2-559351); *fgf18* (C3-123572); *axin2* (C1-465351);
571 *gli1* (C2-542721); *prrx1* (C3-535321); *tnmd* (C1-564481); *scx* (C2-564451); *grem1a*
572 (C1-535291) probes were designed and synthesized by the manufacturer. The
573 universal negative control with probes targeting dapB gene (320871) provided by ACD
574 was used as reference. Double labeling was performed following the manufacturer's

575 instructions. The probes were incubated for 2 hrs at 40°C, with a dilution of 1/50 for
576 each probe. Opal 570 (Akoya, Cat. No. FP1488001KT) and Opal 650 (Akoya, Cat. No.
577 FP1496001KT) each diluted to 1:500 were used to reveal the C1 and C2 or C3 probes,
578 respectively. The slides were mounted using ProLong™ Gold antifade reagent
579 (Invitrogen). These experiments were imaged with a Spinning Disk Zeiss controlled by
580 Zen Blue software (Olympus, Tokyo, Japan) and processed on the Fiji software
581 (ImageJ) to combine all the images into one containing the maximum intensity
582 information for each pixel. The quantitative analysis was performed on two adjacent
583 sections for at least n=6 per genotype, the results show the mean of the two sections
584 and represent the ratio between the number of dots (representing mRNA strands) and
585 the number of cells (DAPI). For the quantitative analysis along the suture, the analyses
586 encompassed all cells within the suture for *fgfr3*$^{+/+}$ fish. In contrast for the *fgfr3*$^{lof/lof}$ fish
587 only cells along the bones within the suture were counted, corresponding to the
588 location of the *runx2:*GFP*, sp7:*mCherry*, bglap:*GFP positive cells labelling. The
589 quantitative analysis along the bone surface correspond to the ratio between the
590 number of dots (mRNA strands) and the number of cells (DAPI) bordering above and
591 below the frontal bones.
592
593 ***Polarization-resolved Second Harmonic Generation microscopy***
594 Multiphoton images of unstained FFPE sections of *fgfr3*$^{+/+}$ (n=6) and *fgfr3*$^{lof/lof}$ (n=6)
595 fish at the 12SL and 26 SL stages were acquired using a custom-built upright laser
596 scanning setup, as previously described [52]. Laser excitation was tuned to 860 nm and
597 excitation power was 2 to 8mW at the sample using a 25x, NA 1.05 water immersion
598 objective (XLPLN-MP, Olympus). Both two-photons excited fluorescence (2PEF) and
599 second harmonic generation (SHG) signals were detected in parallel in two trans-
600 detection channels. Endogenous 2PEF enabled to visualize the tissue morphology,
601 while SHG was obtained specifically from collagen fibrils. Polarization-resolved SHG
602 imaging (P-SHG) was performed by recording series of images excited by linear
603 polarizations rotated from 0° to 170° in 10° steps [52]. Z-stacks of such P-SHG images
604 were recorded at 200 kHz with an axial step of 0.5µm and a pixel size of 420nm.
605 Automated processing by custom written Matlab code then provided: (i) the 2PEF and
606 SHG images averaged over all excitation polarizations, which mitigates the polarization
607 sensitivity; (ii) a pixel-scale orientation map of collagen fibre orientation within the
608 imaging plane [52]. The latter map was obtained after applying a 2x2 binning filter to

609 increase the signal-to-noise ratio. Pixels with a coefficient of determination less than
610 0.5 were filtered out [52].
611 Two quantitative parameters were then calculated from these data, keeping only the
612 image from each z-stack that have the highest mean SHG signal. First, the collagen
613 density within the frontal bone was estimated by calculating the mean intensity of the
614 SHG image normalized to the square of the excitation power. Second, the orientation
615 order of the collagen fibres was quantified by computing the circular standard deviation
616 of the orientation distribution obtained from P-SHG images. This disorder metric
617 assesses the width of the orientation distribution using circular statistics; it increases
618 when the orientation disorder increases. To account for the variation of overall
619 orientation of the bone that would bias a measure of absolute local orientation, this
620 circular standard deviation was computed using the P-SHG orientation relative to the
621 orientation of the bone structure, by computing the direction of the frontal bone locally
622 and eliminating small outgrowths.
623
624 ***Transmission Electron Microscopy***
625 Calvaria from zebrafish at 9, 12 and 20 SL were dissected inside the fixation buffer (for
626 50mL: 10mL of cacodylate 0.5M, 75µL of glutaraldehyde, 12.5mL of PFA 4% qsp 50mL
627 H_2O). The calvarias were left at least 5 days inside the fixation buffer at 4°C and
628 washed 3 times 15 minutes in PBS, then decalcified 24 hrs in EDTA 0.5M pH8 at 4°C.
629 Samples were post fixed in 1% osmium tetroxide 0.1M (Electron Microscopy Science,
630 UK) in 0.1 M Phosphate Buffer (PB) (pH 7.4). Samples were washed 3 times in H_2O
631 then dehydrated in alcohol grades: 70% Ethanol 10 min, 90% Ethanol 10 min, 100%
632 Ethanol 3x15min, 100% Propylene oxide (Electron Microscopy Science, UK) 2x5 min.
633 Resin infiltration was performed as following: mix 1:1 Epikote 812: propylene oxide 30
634 min followed by mix 1:2 Epikote 812: propylene oxide overnight room temperature.
635 Samples were washed in 100% Epikote 812 then embedded in silicon molds in 100%
636 Epikote 812, and Polymerised in a 60°C oven for 24 hours. Ultrathin sections were cut
637 at 90 nm with a Leica UFC7 ultramicrotome (Leica Microsystems GmbH, Germany)
638 and deposed on Gilder grids 200 mesh (Electron Microscopy Science, UK). They were
639 counterstained with uranyl acetate 7% (LFG, France) and Reynold's lead citrate (LFG,
640 France). Samples were examined in a JEOL 1011 transmission electron microscope
641 (JEOL, Japan) with an ORIUS 1000 CCD camera (GATAN, France), operated with
642 Digital Micrograph software (GATAN, France) for acquisition.

643 ***Statistical analysis***

644 All statistical analyses were performed using GraphPad Prism (version 10, GraphPad
645 Software, La Jolla, CA, USA). Data normality and lognormality were assessed using
646 the D'Agostino & Pearson, Anderson-Darling, Shapiro-Wilk, and Kolmogorov-Smirnov
647 tests. For data following a normal distribution, statistical comparisons were performed
648 using an unpaired t-test when analysing an independent variable between two groups.
649 A two-way ANOVA was used to assess statistically significant differences between
650 three or more independent groups split across two variables. Non-normally distributed
651 data were analysed using a non-parametric Mann-Whitney test for two-group
652 comparisons. A significance threshold of $p < 0.05$ was applied to all statistical tests. p-
653 values reported in figure legends were considered statistically significant as follows: *,
654 $p < 0.05$; **, $p < 0.01$; ***, $p < 0.001$; and ****, $p < 0.0001$. All values are presented as
655 mean ± SD.
656

657 **Acknowledgments**

658 We are grateful to Dr Chrissy Hammond for providing the Tg(*col2*:mCherry) fish
659 line, Dr Shahad Albadri for the Tg(*7xTCF-Xla.Siam*:GFP), Dr Gilbert Weidinger for
660 providing the Tg(*sp7*:mCherry) and Tg(*bglap*:GFP) fish lines and the members of the
661 fish-facility in the Institut Imagine. We thank all the members of the Institut Imagine Cell
662 Imaging and animal facility. We are grateful to the histology core facility of the Structure
663 Fédérative de Recherche Necker. We thank Paolo Bonaldo for generously providing
664 the antibody against Col VI. We thank Drs. Chris Gordon, Marion Coolen and Sophie
665 Thomas for their valuable advice in writing this manuscript. With regard to funding, this
666 work was supported by ANR-21-CE14-0010 "STARFISH" from the Agence Nationale
667 de le Recherche. We thank the Philanthropy Department of Mutuelles AXA through the
668 "Head and Heart Chair" for supporting the Imagine Institute's imaging facility. MCSK,
669 AC and YL acknowledge funding from the "Agence Nationale de la Recherche" (ANR-
670 10-INBS-04, ANR-11-EQPX-0029). We thank the ARC Foundation for Cancer
671 Research for the acquisition of the nanozoomer at the histology core facility.
672
673
674

Authors' roles:

RP designed the experiments, contributed to the acquisition of data, analysed the data and wrote the paper. YM contributed to the acquisition of data. YL and CA contributed to analysis of SHG data. SA and MM contributed to the acquisition of TEM data. MCSK conceived the SHG study, contributed to analysis SHG data and preparation of the paper. FR contributed to analysis of ECM data and preparation of the paper. LLM contributed to analysis of data and preparation of the paper. ED conceived the study, contributed to the analysis of the data and wrote the paper. All authors reviewed the paper and provided intellectual content**.**

Competing interest statement:

The authors have declared no competing interest.

689 1. Twigg, S. R. F. & Wilkie, A. O. M. A Genetic-Pathophysiological Framework for Craniosynostosis.
690 *Am J Hum Genet* **97**, 359–377 (2015).
691 2. Cornille, M. *et al.* Animal models of craniosynostosis. *Neurochirurgie* **65**, 202–209 (2019).
692 3. Lana-Elola, E., Rice, R., Grigoriadis, A. E. & Rice, D. P. C. Cell fate specification during calvarial
693 bone and suture development. *Developmental Biology* **311**, 335–346 (2007).
694 4. Holmes, G. *et al.* Integrated Transcriptome and Network Analysis Reveals Spatiotemporal
695 Dynamics of Calvarial Suturogenesis. *Cell Reports* **32**, 107871 (2020).
696 5. Farmer, D. T. *et al.* Cellular transitions during cranial suture establishment in zebrafish. *Nat*
697 *Commun* **15**, 6948 (2024).
698 6. Maruyama, T., Jeong, J., Sheu, T.-J. & Hsu, W. Stem cells of the suture mesenchyme in
699 craniofacial bone development, repair and regeneration. *Nat Commun* **7**, 10526 (2016).
700 7. Zhao, H. *et al.* The suture provides a niche for mesenchymal stem cells of craniofacial bones. *Nat*
701 *Cell Biol* **17**, 386–396 (2015).
702 8. Maruyama, T. *et al.* BMPR1A maintains skeletal stem cell properties in craniofacial development
703 and craniosynostosis. *Sci. Transl. Med.* **13**, eabb4416 (2021).
704 9. Wilk, K. *et al.* Postnatal Calvarial Skeletal Stem Cells Expressing PRX1 Reside Exclusively in the
705 Calvarial Sutures and Are Required for Bone Regeneration. *Stem Cell Reports* **8**, 933–946 (2017).
706 10. Debnath, S. *et al.* Discovery of a periosteal stem cell mediating intramembranous bone
707 formation. *Nature* **562**, 133–139 (2018).
708 11. Teng, C. S. *et al.* Altered bone growth dynamics prefigure craniosynostosis in a zebrafish model
709 of Saethre-Chotzen syndrome. *Elife* **7**, e37024 (2018).
710 12. Bok, S. *et al.* A multi-stem cell basis for craniosynostosis and calvarial mineralization. *Nature* **621**,
711 804–812 (2023).
712 13. Herring, S. W. Mechanical influences on suture development and patency. *Front Oral Biol* **12**, 41–
713 56 (2008).

714 14. Izu, Y., Ezura, Y., Koch, M., Birk, D. E. & Noda, M. Collagens VI and XII form complexes mediating
715 osteoblast interactions during osteogenesis. *Cell Tissue Res* **364**, 623–635 (2016).
716 15. Izu, Y. *et al.* Type XII collagen regulates osteoblast polarity and communication during bone
717 formation. *J Cell Biol* **193**, 1115–1130 (2011).
718 16. Huang, X. *et al.* Gli1+ Cells Residing in Bone Sutures Respond to Mechanical Force via IP3R to
719 Mediate Osteogenesis. *Stem Cells Int* **2021**, 8138374 (2021).
720 17. Jing, D. *et al.* Response of Gli1+ Suture Stem Cells to Mechanical Force Upon Suture Expansion. *J*
721 *Bone Miner Res* **37**, 1307–1320 (2022).
722 18. Daponte, V. *et al.* Cell differentiation and matrix organization are differentially affected during
723 bone formation in osteogenesis imperfecta zebrafish models with different genetic defects
724 impacting collagen type I structure. *Matrix Biol* **121**, 105–126 (2023).
725 19. Ga, M., Sj, O., Ir, M., Ka, P. & Ew, J. Fibroblast growth factor receptor 3 (FGFR3) transmembrane
726 mutation in Crouzon syndrome with acanthosis nigricans. *Nature genetics* **11**, (1995).
727 20. Muenke, M. *et al.* A unique point mutation in the fibroblast growth factor receptor 3 gene
728 (FGFR3) defines a new craniosynostosis syndrome. *Am J Hum Genet* **60**, 555–564 (1997).
729 21. Makrythanasis, P. *et al.* A novel homozygous mutation in FGFR3 causes tall stature, severe lateral
730 tibial deviation, scoliosis, hearing impairment, camptodactyly, and arachnodactyly. *Hum. Mutat.*
731 **35**, 959–963 (2014).
732 22. Deng, C., Wynshaw-Boris, A., Zhou, F., Kuo, A. & Leder, P. Fibroblast growth factor receptor 3 is a
733 negative regulator of bone growth. *Cell* **84**, 911–921 (1996).
734 23. Nah, H.-D., Koyama, E., Agochukwu, N. B., Bartlett, S. P. & Muenke, M. Phenotype profile of a
735 genetic mouse model for Muenke syndrome. *Childs Nerv Syst* **28**, 1483–1493 (2012).
736 24. Cornille, M. *et al.* FGFR3 overactivation in the brain is responsible for memory impairments in
737 Crouzon syndrome mouse model. *J Exp Med* **219**, e20201879 (2022).

738 25. Laue, K. *et al.* Craniosynostosis and multiple skeletal anomalies in humans and zebrafish result
739 from a defect in the localized degradation of retinoic acid. *Am. J. Hum. Genet.* **89**, 595–606
740 (2011).
741 26. Pereur, R. & Dambroise, E. Insights into Craniofacial Development and Anomalies: Exploring Fgf
742 Signaling in Zebrafish Models. *Curr Osteoporos Rep* **22**, 340–352 (2024).
743 27. Sun, X. *et al.* Fgfr3 mutation disrupts chondrogenesis and bone ossification in zebrafish model
744 mimicking CATSHL syndrome partially via enhanced Wnt/β-catenin signaling. *Theranostics* **10**,
745 7111–7130 (2020).
746 28. Dambroise, E. *et al.* Fgfr3 Is a Positive Regulator of Osteoblast Expansion and Differentiation
747 During Zebrafish Skull Vault Development. *J Bone Miner Res* **35**, 1782–1797 (2020).
748 29. Izu, Y. & Birk, D. E. Collagen XII mediated cellular and extracellular mechanisms in development,
749 regeneration, and disease. *Front. Cell Dev. Biol.* **11**, 1129000 (2023).
750 30. Miao, K. Z., Cozzone, A., Caetano-Lopes, J., Harris, M. P. & Fisher, S. Osteoclast activity sculpts
751 craniofacial form to permit sensorineural patterning in the zebrafish skull. *Front. Endocrinol.* **13**,
752 969481 (2022).
753 31. Farmer, D. T. *et al.* The developing mouse coronal suture at single-cell resolution. *Nat Commun*
754 **12**, 4797 (2021).
755 32. Moshkovsky, A. R. & Kirschner, M. W. The nonredundant nature of the Axin2 regulatory network
756 in the canonical Wnt signaling pathway. *Proc. Natl. Acad. Sci. U.S.A.* **119**, e2108408119 (2022).
757 33. Bobzin, L. *et al.* FGFR2 directs inhibition of WNT signaling to regulate anterior fontanelle closure
758 during skull development. *Development* **152**, dev204264 (2025).
759 34. Di Rocco, F. *et al.* FGFR3 mutation causes abnormal membranous ossification in achondroplasia.
760 *Hum. Mol. Genet.* **23**, 2914–2925 (2014).
761 35. Kague, E. *et al.* Osterix/Sp7 limits cranial bone initiation sites and is required for formation of
762 sutures. *Dev. Biol.* **413**, 160–172 (2016).

763 36. Katsianou, M. A., Adamopoulos, C., Vastardis, H. & Basdra, E. K. Signaling mechanisms implicated
764 in cranial sutures pathophysiology: Craniosynostosis. *BBA Clinical* **6**, 165–176 (2016).
765 37. Jiang, T., Ge, S., Shim, Y. H., Zhang, C. & Cao, D. Bone morphogenetic protein is required for
766 fibroblast growth factor 2-dependent later-stage osteoblastic differentiation in cranial suture
767 cells. *Int J Clin Exp Pathol* **8**, 2946–2954 (2015).
768 38. Warren, S. M., Brunet, L. J., Harland, R. M., Economides, A. N. & Longaker, M. T. The BMP
769 antagonist noggin regulates cranial suture fusion. *Nature* **422**, 625–629 (2003).
770 39. Matsushita, T. *et al.* FGFR3 promotes synchondrosis closure and fusion of ossification centers
771 through the MAPK pathway. *Hum. Mol. Genet.* **18**, 227–240 (2009).
772 40. Ng, J. Q. *et al.* Loss of Grem1-lineage chondrogenic progenitor cells causes osteoarthritis. *Nat*
773 *Commun* **14**, 6909 (2023).
774 41. Ohbayashi, N. *et al.* FGF18 is required for normal cell proliferation and differentiation during
775 osteogenesis and chondrogenesis. *Genes Dev.* **16**, 870–879 (2002).
776 42. Menon, S. *et al.* Skeletal stem and progenitor cells maintain cranial suture patency and prevent
777 craniosynostosis. *Nat Commun* **12**, 4640 (2021).
778 43. Mirando, A. J., Maruyama, T., Fu, J., Yu, H.-M. I. & Hsu, W. β-catenin/cyclin D1 mediated
779 development of suture mesenchyme in calvarial morphogenesis. *BMC Dev Biol* **10**, 116 (2010).
780 44. Reinhold, M. I. & Naski, M. C. Direct interactions of Runx2 and canonical Wnt signaling induce
781 FGF18. *J Biol Chem* **282**, 3653–3663 (2007).
782 45. Gregory, C. A., Ma, J. & Lomeli, S. The coordinated activities of collagen VI and XII in maintenance
783 of tissue structure, function and repair: evidence for a physical interaction. *Front. Mol. Biosci.* **11**,
784 1376091 (2024).
785 46. Izu, Y. *et al.* Collagen XII mediated cellular and extracellular mechanisms regulate establishment
786 of tendon structure and function. *Matrix Biology* **95**, 52–67 (2021).

787 47. Parichy, D. M., Elizondo, M. R., Mills, M. G., Gordon, T. N. & Engeszer, R. E. Normal table of
788 postembryonic zebrafish development: staging by externally visible anatomy of the living fish.
789 *Dev. Dyn.* **238**, 2975–3015 (2009).
790 48. Knopf, F. *et al.* Bone regenerates via dedifferentiation of osteoblasts in the zebrafish fin. *Dev. Cell*
791 **20**, 713–724 (2011).
792 49. Moro, E. *et al.* In vivo Wnt signaling tracing through a transgenic biosensor fish reveals novel
793 activity domains. *Dev Biol* **366**, 327–340 (2012).
794 50. Tonelotto, V. *et al.* Collagen VI ablation in zebrafish causes neuromuscular defects during
795 developmental and adult stages. *Matrix Biol* **112**, 39–61 (2022).
796 51. Bader, H. L. *et al.* Zebrafish collagen XII is present in embryonic connective tissue sheaths (fascia)
797 and basement membranes. *Matrix Biol* **28**, 32–43 (2009).
798 52. Raoux, C. *et al.* Quantitative structural imaging of keratoconic corneas using polarization-
799 resolved SHG microscopy. *Biomed Opt Express* **12**, 4163–4178 (2021).
800

801 **Figure 1. Fgfr3 is required for cranial vault suture formation.** (A) Schematic
802 representation of the zebrafish cranial vault. The dotted arrow corresponds to the plane
803 of sectioning. (B) *fgfr3* expression (red) on whole mount *fgfr3*$^{+/+}$ cranial vault at 10 SL
804 labelled by RNAscope *in situ* hybridization showed the high expression of *fgfr3* at the
805 periphery of cranial bones and in the forming sutures. F= Frontal bone, P= Parietal
806 bone, O= Occipital bone. Scale bar = 300 µm. (C) *fgfr3* expression (red) on coronal
807 sections of *fgfr3*$^{+/+}$ metopic suture at 12 SL and 20 SL labelled by RNAscope *in situ*
808 hybridization. At both stages, *fgfr3* was expressed in cells along the bone surface and
809 within the suture. Nuclei were counterstained with DAPI (blue). Scale bar = 50 µm. (D)
810 RNAscope, quantitative analyses of the number of transcript (dot) relative to the
811 number of nuclei (DAPI) highlighted that at 12 SL *fgfr3* was more highly expressed
812 inside the suture compared to the bone surface. In contrast, at 20 SL, no difference of
813 *fgfr3* expression was observed based on localisation (12 SL and 20 SL: *fgfr3*$^{+/+}$ n=6;
814 *fgfr3*$^{lof/lof}$ n=6). (E) HE stained coronal sections of the zebrafish head at the metopic
815 suture level at 12, 20 and 26 SL demonstrated that the absence of Fgfr3 induced a
816 delay of frontal bone growth, and prevented frontal bones overlap at 20 and 26 SL.
817 The dotted lines represent the bone boundaries. Scale bar = 50 µm. (F) Quantification
818 of the number of cells inside the suture at 20 SL (*fgfr3*$^{+/+}$ n=14; *fgfr3*$^{lof/lof}$ n=14) and 26
819 SL (*fgfr3*$^{+/+}$ n=17; *fgfr3*$^{lof/lof}$ n=11) showed that the *fgfr3*$^{lof/lof}$ fish present a greater
820 number of cells within the suture at adulthood. (G) Measurement of frontal bone
821 thickness close to the metopic suture at 12 SL (*fgfr3*$^{+/+}$ n=6; *fgfr3*$^{lof/lof}$ n=6), 20 SL
822 (*fgfr3*$^{+/+}$ n=6; *fgfr3*$^{lof/lof}$ n=8) and 26 SL (*fgfr3*$^{+/+}$ n=10; *fgfr3*$^{lof/lof}$ n=9) showed that the
823 *fgfr3*$^{lof/lof}$ bones are thicker than *fgfr3*$^{+/+}$ bones at adulthood. F: frontal bone. Data are
824 presented as mean ± SD. The p-values were determined by Student's t tests: ns: not
825 significant; $p < 0.05$ = *; $p < 0.01$ = **; $p < 0.001$ = ***.
826
827 **Figure 2**. **Fgfr3 deficiency leads to disruption of fibrillogenesis within the suture**
828 **at adulthood.** (A) Sirius Red–Alcian Blue stained coronal sections of the zebrafish
829 head at the metopic suture level at 12 and 20 SL demonstrated that the absence of
830 Fgfr3 induced an accumulation and a disorganization of the suture ECM at 20 SL. The
831 dotted lines represent the bone boundaries. Scale bar = 50 µm. (B-D)
832 Immunofluorescence against ColI (B), ColXII (C) and ColVI (D) on metopic sutures of
833 *fgfr3*$^{+/+ \text{ or } lof/lof}$ fish at 12 and 20 SL showed a higher amount of ColI and ColXII within
834 the suture of the *fgfr3*$^{lof/lof}$ fish. Nuclei were counterstained with DAPI (blue) and the

835 dotted lines represent the bone boundaries. Scale bar = 50 µm. (12 SL: ColI: *fgfr3*$^{+/+}$
836 n=3; *fgfr3*$^{lof/lof}$ n=5; ColVI: *fgfr3*$^{+/+}$ n=7; *fgfr3*$^{lof/lof}$ n=5; ColXII: *fgfr3*$^{+/+}$ n=3; *fgfr3*$^{lof/lof}$ n=3)
837 (20 SL: ColI: *fgfr3*$^{+/+}$ n=3; *fgfr3*$^{lof/lof}$ n=3; ColXI: *fgfr3*$^{+/+}$ n=5; *fgfr3*$^{lof/lof}$ n=5; ColXII: *fgfr3*$^{+/+}$
838 n=3; *fgfr3*$^{lof/lof}$ n=3). (E) Coronal sections of 9, 12 and 20 SL fish imaged by transmission
839 electron microscopy. Scale bar = 0.5 µm. (F) Measurement of fibril transverse area
840 distribution within the suture at 19, 12, and 20 SL revealed a more heterogeneous fibril
841 size in *fgfr3*$^{lof/lof}$ compared to controls. (G) Comparison of the mean fibril transverse
842 area in the metopic suture of *fgfr3*$^{+/+ \text{ and } lof/lof}$ fish revealed an increase in fibril size in the
843 mutants at 20 SL (9 SL: (*fgfr3*$^{+/+}$ n=3; *fgfr3*$^{lof/lof}$ n=2) (12 SL: (*fgfr3*$^{+/+}$ n=3; *fgfr3*$^{lof/lof}$ n=3)
844 (20 SL: (*fgfr3*$^{+/+}$ n=2; *fgfr3*$^{lof/lof}$ n=2). F: Frontal bone. Data are presented as mean ± SD.
845 The p-value was determined by a Student's t test: $p < 0.05$ = *.
846
847 **Figure 3. Loss of Fgfr3 affected the organization of bone collagen fibers at the**
848 **bone ends over time** (A) Diagrams representing the different areas analysed by SHG
849 microscopy. Zone 1 corresponds to the bone surrounding the suture called the bones
850 ends, while zone 2 refers to bone located farther away. (B) Coronal sections of metopic
851 suture at 12 and 26 SL imaged by SHG microscopy at 12 and 26 SL. Scale bar = 50
852 µm. The color codes for the collagen orientation as shown by the color wheel in the
853 inset. (C-D) Quantification of the SHG intensity normalized to the excitation power
854 squared (SHG_{norm}) and of the circular standard deviation of the collagen orientation
855 distribution (orientation SD) in zone 1 and 2 at 12 SL (C) and 26 SL (D). In zone 1, the
856 circular standard deviation of the collagen orientation distribution is significantly higher
857 in *fgfr3*$^{lof/lof}$ at 26 SL, suggesting a disorganization of the collagen fibers at the ends of
858 the frontal bones (12 SL: *fgfr3*$^{+/+}$ n=6; *fgfr3*$^{lof/lof}$ n=6) (26 SL: *fgfr3*$^{+/+}$ n=6; *fgfr3*$^{lof/lof}$
859 n=6).Data are presented as mean ± SD. The p-values were determined by Student's t
860 tests: ns: not significant; $p < 0,05$ = *.
861
862 **Figure 4. Fgfr3 prevents osteoprogenitor expansion, and activates osteoblast**
863 **maturation within the metopic suture** (A) Immunofluorescence against GFP (green)
864 performed on metopic sutures of *Tg(runx2:GFP*; *fgfr3*$^{+/+ \text{ or } lof/lof}$) fish at 12 and 20 SL.
865 Scale bar = 50 µm (B) Immunofluorescence against GFP (green) and mCherry (red)
866 was performed on metopic sutures of *Tg(sp7:mCherry; bglap:GFP*; *fgfr3*$^{+/+ \text{ or } lof/lof}$) fish
867 at 12 and 20SL. Scale bar = 50 µm. (C) Quantification at 20 SL of the percentage of
868 osteoprogenitors along the suture revealed a significantly higher number of

869 osteoprogenitors in the *fgfr3*$^{lof/lof}$ suture compared to the control (*fgfr3*$^{+/+}$ n=6; *fgfr3*$^{lof/lof}$
870 n=6). The p-value was determined by a two-way ANOVA. (D-E) Quantification at 20
871 SL of the percentage of *sp7*:mCherry positive cells and *bglap*:GFP positive cells along
872 the suture and the bone surface revealed a greater number of immature osteoblasts
873 and a drastically lower number of mature osteoblasts at the edge of the *fgfr3*$^{lof/lof}$
874 metopic suture compared to controls. No significant difference was observed along the
875 bone surface. (*fgfr3*$^{+/+}$ n=5; *fgfr3*$^{lof/lof}$ n=6). The p-values were determined by a two-way
876 ANOVA. (F) EdU assays performed on *fgfr3*$^{+/+\ or\ lof/lof}$ metopic suture at 12 and 20 SL.
877 (G) TUNEL assays labelling apoptotic cells performed on *fgfr3*$^{+/+}$ and *fgfr3*$^{lof/lof}$ metopic
878 suture at 12, 20 and 26 SL fish. Scale bar = 50 µm. (H) Quantification of the percentage
879 of EdU positive cells revealed no significant defect of proliferation at 12 and 20 SL on
880 *fgfr3*$^{lof/lof}$ sutures (12 SL: *fgfr3*$^{+/+}$ n=5; *fgfr3*$^{lof/lof}$ n=6; 20 SL: *fgfr3*$^{+/+}$ n=6; *fgfr3*$^{lof/lof}$ n=6). p-
881 values were determined by Student's t tests. (I) Quantitative analysis of apoptotic cell
882 percentages, relative to the number of nuclei stained with DAPI, revealed a significantly
883 higher incidence of apoptosis in the *fgfr3*$^{lof/lof}$ suture compared to *fgfr3*$^{+/+}$ at 20 and 26
884 SL (20 SL: *fgfr3*$^{+/+}$ n=8; *fgfr3*$^{lof/lof}$ n=8; 26 SL: *fgfr3*$^{+/+}$ n=9; *fgfr3*$^{lof/lof}$ n=8). p-values were
885 determined by Student's t tests. Nuclei were counterstained with DAPI (blue) and the
886 dotted lines represent the bones boundary. F: Frontal bone. Data are presented as
887 mean ± SD. ns: not significant; p < 0,05 = *; p < 0,01 = **; p < 0,001 = ***; p < 0,0001
888 = ****.
889
890 **Figure 5. The absence of Fgfr3 alters the SuSC marker profile, highlighting the**
891 **downregulation of the BMP antagonist Grem1 and the activation of the Wnt**
892 **signaling pathway within the suture** (A) Expression of *prrx1, gli1, axin2*, and *grem1*
893 (red) in coronal sections of the metopic suture at 12 and 20 SL, labeled by RNAscope
894 in situ hybridization. Nuclei are counterstained with DAPI (blue). Scale bar = 50 µm.
895 (B) Quantitative RNAscope analysis revealed increased expression of *gli1* and *axin2*
896 in *fgfr3*$^{lof/lof}$ metopic sutures compared to controls. In contrast, *grem1* expression is
897 significantly reduced at 20 SL. (12 SL: *fgfr3*$^{+/+}$ n=6; *fgfr3*$^{lof/lof}$ n=6; 20 SL: *fgfr3*$^{+/+}$ n=7;
898 *fgfr3*$^{lof/lof}$ n=7). p-values were determined by two-way ANOVA. (C) Quantitative
899 RNAscope analysis of *axin2* expression along the metopic suture edge demonstrated
900 higher *axin2* expression in *fgfr3*$^{lof/lof}$ fish compared to controls at both 12 and 20 SL (12
901 SL: *fgfr3*$^{+/+}$ n=6; *fgfr3*$^{lof/lof}$ n=6; 20 SL: *fgfr3*$^{+/+}$ n=7; *fgfr3*$^{lof/lof}$ n=7). p-values were
902 determined by two-way ANOVA. (D) Immunofluorescence against GFP (green) was

903 performed on metopic sutures of Tg(7xTCF-Xla.Siam:GFP; *fgfr3*$^{+/+\ or\ lof/lof}$) fish at 12
904 SL. (E) Quantification at 12 SL of the number GFP-positive cells revealed a significantly
905 higher number of cells at the tips of *fgfr3*$^{lof/lof}$ bones compared to controls, suggesting
906 an overactivation of the Wnt signaling pathway (*fgfr3*$^{+/+}$ n=5; *fgfr3*$^{lof/lof}$ n=7). p-values
907 were determined by Student's t-test: ns = not significant; $p < 0.05$ = *; $p < 0.01$ = **; p
908 < 0.001 = ***; p < 0.0001 = ****. Data are presented as mean ± SD.
909
910 **Figure 6. The absence of Fgfr3 is not compensated by other Fgfrs and leads to**
911 **the overexpression of Fgf18 within the suture** (A) *fgf2* and *fgf18* expression (red)
912 on coronal sections of metopic suture at 12 and 20 SL labelled by RNAscope *in situ*
913 hybridization. Nuclei were counterstained with DAPI (blue). Scale bar = 50 µm. The
914 dotted lines represent the bone boundaries. (B-C) RNAscope Quantitative analyses of
915 *fgf2* and *fgf18* expression in *fgfr3*$^{+/+}$ versus *fgfr3*$^{lof/lof}$ within the suture (B) or along the
916 bone surface (C) at 12 and 20 SL showed that *fgf18* is significantly more expressed in
917 the *fgfr3*$^{lof/lof}$ suture than in *fgfr3*$^{+/+}$ suture at 12 and 20 SL (12 SL and 20 SL: *fgfr3*$^{+/+}$
918 n=6; *fgfr3*$^{lof/lof}$ n=6). (D, E) *fgfr1a, fgfr1b* and *fgfr2* expression (red) on coronal sections
919 of metopic suture at 12 and 20 SL labelled by RNAscope *in situ* hybridization. Nuclei
920 were counterstained with DAPI (blue). Scale bar = 50 µm. The dotted lines represent
921 the bone boundaries. (F, G) RNAscope quantitative analyses of *fgfr1a, fgfr1b* and *fgfr2*
922 expression in *fgfr3*$^{+/+}$ versus *fgfr3*$^{lof/lof}$ within the suture (F) or along the bone surface
923 (G) at 12 and 20 SL revealed similar expression of *fgfr1a, fgfr1b*, and *fgfr2* in both
924 genotypes. (12 SL: *fgfr3*$^{+/+}$ n=6; *fgfr3*$^{lof/lof}$ n=6; 20 SL: *fgfr3*$^{+/+}$ n=7; *fgfr3*$^{lof/lof}$ n=7). Data
925 are presented as mean ± SD. p-values were determined by two-way ANOVA: ns: not
926 significant; $p < 0,05$ = *; $p < 0,01$ = **.
927
928 **Figure 7. Impact of Fgfr3 absence on cranial suture formation**
929 The absence of FGFR3 exerts pleiotropic effects on cranial suture formation, leading
930 to significant structural defects. Without Fgfr3, proper overlap of the sutures is
931 prevented, resulting in bone widening. These structural abnormalities are associated
932 with osteogenesis defects, as Fgfr3 deficiency disrupts the expansion of
933 osteoprogenitors within the suture and hinders bone maturation, thereby inhibiting
934 longitudinal bone growth. Additionally, the absence of Fgfr3 affects the extracellular
935 matrix (ECM) at the ends of bones and within the suture itself. From a signaling
936 pathway perspective, the loss of Fgfr3 triggers the overexpression of Fgf18 and causes

937 the misregulation of *axin2* and *grem1* expression. This positions Fgfr3 as a central
938 regulator of cranial suture formation in a complex network involving FGF, BMP, and
939 Wnt signaling pathways.
940
941 **Supplementary data**
942
943 **Figure 1 supplement 1.** Fgfr3 is required for coronal suture formation. (A) HE stained
944 sagittal sections of the zebrafish head at the coronal suture level at 20 SL
945 demonstrated that the absence of Fgfr3 prevents bones overlap and coronal suture
946 formation. The dotted lines represent the bone boundaries. Scale bar = 50 µm. (B)
947 Measurement of bone thickness near the coronal suture showed that the *fgfr3*$^{lof/lof}$
948 bones are thicker than *fgfr3*$^{+/+}$ bones at the adult stages 20 SL (*fgfr3*$^{+/+}$ n=6; *fgfr3*$^{lof/lof}$
949 n=6) and 26 SL (*fgfr3*$^{+/+}$ n=7; *fgfr3*$^{lof/lof}$ n=6). F: frontal bone. P: Parietal bone. Data are
950 presented as mean ± SD. The p-value were determined by Student's t tests: ns: not
951 significant; $p < 0.05$ = *; $p < 0.01$ = **; $p < 0.001$ = ***; $p < 0.0001$ = ****.
952
953 **Figure 4 supplement 1.**TRAP-stained sagittal sections of the zebrafish head revealed
954 that TRAP positive cells are present on the viscerocranium (A) and the absence of
955 TRAP positive cells within the metopic suture (B) in both *fgfr3*$^{lof/lof}$ and *fgfr3*$^{+/+}$ zebrafish
956 at 12, 20 and 26 SL. The dotted lines represent the bone boundaries. F: Frontal bone.
957 Scale bar = 50 µm.
958
959 **Figure 4 supplement 2.** Fgfr3 is an inhibitor of osteoprogenitors expansion within the
960 suture. The nuclei of cells along the suture in *fgfr3*$^{lof/lof}$ fish exhibit the shape of
961 osteoprogenitor nuclei. (A) Schematic representation of *fgfr3*$^{+/+}$ and *fgfr3*$^{lof/lof}$ metopic
962 sutures indicating the different zones studied. (B) High magnification of nuclei stained
963 with DAPI at the osteogenic front (OF) and along the metopic suture of 20 SL
964 *Tg(runx2:GFP*; *fgfr3*$^{+/+ \text{ or } lof/lof}$) fish. Scale bar = 5 µm. (C) Coronal sections of 20 SL
965 fish imaged by transmission electron microscopy. The dotted lines represent the
966 nuclear boundaries. Scale bar = 2 µm. (D) Quantitative comparison between the
967 nucleus of *fgfr3*$^{+/+}$ cells along the suture and the OF and of *fgfr3*$^{lof/lof}$ cells along the
968 sutures (*fgfr3*$^{+/+}$ n=6; *fgfr3*$^{lof/lof}$ n=6). The nuclear shape of *fgfr3*$^{lof/lof}$ cells along the suture
969 is similar to that of OF cells in the controls, and not to that of cells at the edge of the

970 metopic suture in the controls. Data are presented as mean ± SD. The p-values were
971 determined by Student's t tests. ns: not significant; $p < 0.05$ = *; $p < 0.01$ = **.
972
973 **Figure 4 supplement 3.** (A) Immunofluorescence against GFP (green) and mCherry
974 (red) was performed on metopic sutures of *Tg(sp7:mCherry; bglap:GFP*; *fgfr3*$^{+/+\ or\ lof/lof}$)
975 fish at 26 SL. Nuclei were counterstained with DAPI (blue) and the dotted lines
976 represent the bone boundaries. Scale bar = 50 µm. (B-C) Quantification at 26 SL of
977 the percentage of *sp7*:mCherry positive cells and *bglap*:GFP positive cells along the
978 suture and along the bone surface (*fgfr3*$^{+/+}$ n=9; *fgfr3*$^{lof/lof}$ n=5). (D) Immunofluorescence
979 against GFP (green) and mCherry (red) was performed on coronal sutures of
980 *Tg(sp7:mCherry; bglap:GFP*; *fgfr3*$^{+/+\ or\ lof/lof}$) fish at 26SL. Nuclei were counterstained
981 with DAPI (blue) and the dotted lines represent the bone boundaries. Scale bar = 50
982 µm. (E-F) Quantification at 26 SL of the percentage of *sp7*:mCherry and *bglap*:GFP
983 positive cells along the coronal suture (*fgfr3*$^{+/+}$ n=5; *fgfr3*$^{lof/lof}$ n=5; except *bglap* along
984 the bone surface *fgfr3*$^{lof/lof}$ n=4). F: Frontal bone. P: Parietal bone. The p-values were
985 determined by two-way ANOVA. ns: not significant; $p < 0.01$ = **; $p < 0.001$ = ***; $p <$
986 0.0001 = ****.
987
988 **Figure 5 supplement 1.**(A) Expression of *tnmd* and *scx* (red) in coronal sections of
989 the metopic suture at 20 SL, labeled by RNAscope *in situ* hybridization. Nuclei are
990 counterstained with DAPI (blue). Scale bar = 50 µm. (B) Quantitative RNAscope
991 analysis revealed that *tnmd* and *scx* are not differentially expressed in *fgfr3*$^{lof/lof}$
992 compared to controls (*tnmd fgfr3*$^{+/+}$ n=8; *fgfr3*$^{lof/lof}$ n=6; *scx fgfr3*$^{+/+}$ n=8; *fgfr3*$^{lof/lof}$ n=7).
993 Data are presented as mean ± SD. F: Frontal bone. p-values were determined by
994 Student's t tests. ns: not significant. The dotted lines represent the bone boundaries.
995
996 **Figure 6 supplement 1.**RNAscope quantitative analyses of *fgfr1a, fgfr1b* and *fgfr2*
997 expression in suture versus bone surface in *fgfr3*$^{+/+}$ or *fgfr3*$^{lof/lof}$ at 12 and 20 SL showed
998 that *fgfr1a is* more highly expressed along the bone surface than within the suture in
999 *fgfr3*$^{lof/lof}$ fish at 12 SL, while *fgfr2* is more highly expressed in bone surface than the
1000 suture at 20 SL, in both genotypes (*fgfr1a* and *fgfr1b*: 12 SL: *fgfr3*$^{+/+}$ n=6; *fgfr3*$^{lof/lof}$ n=6;
1001 20 SL: *fgfr3*$^{+/+}$ n=7; *fgfr3*$^{lof/lof}$ n=6) (*fgfr2*: 12 SL: *fgfr3*$^{+/+}$ n=6; *fgfr3*$^{lof/lof}$ n=6; 20 SL: *fgfr3*$^{+/+}$
1002 n=7; *fgfr3*$^{lof/lof}$ n=7). Data are presented as mean ± SD. The p-values were determined

1003 by two-way ANOVA. ns: not significant; $p < 0.01$ = **; $p < 0.001$ = ***; $p < 0.0001$ = ****.

1004 The dotted lines represent the bone boundaries.

1005

1006

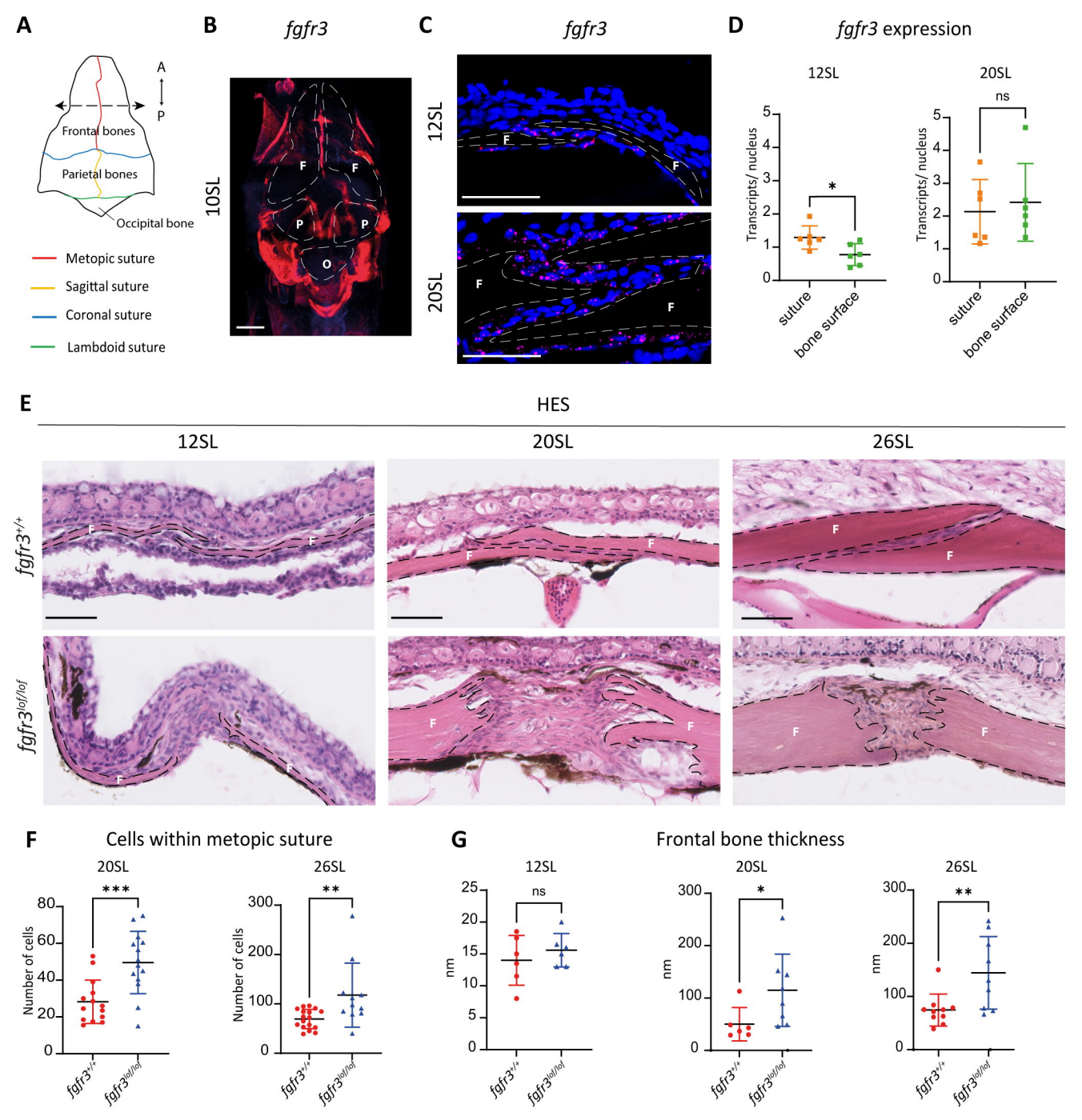
A
A
P
Frontal bones
Parietal bones
Occipital bone
Metopic suture
Sagittal suture
Coronal suture
Lambdoid suture
B
fgfr3
10SL
F
F
P
P
O
C
fgfr3
12SL
20SL
F
F
F
F
D
fgfr3 expression
12SL
20SL
Transcripts/ nucleus
*
ns
suture
bone surface
E
HES
12SL
20SL
26SL
fgfr3+/+
fgfr3lof/lof
F
F
F
F

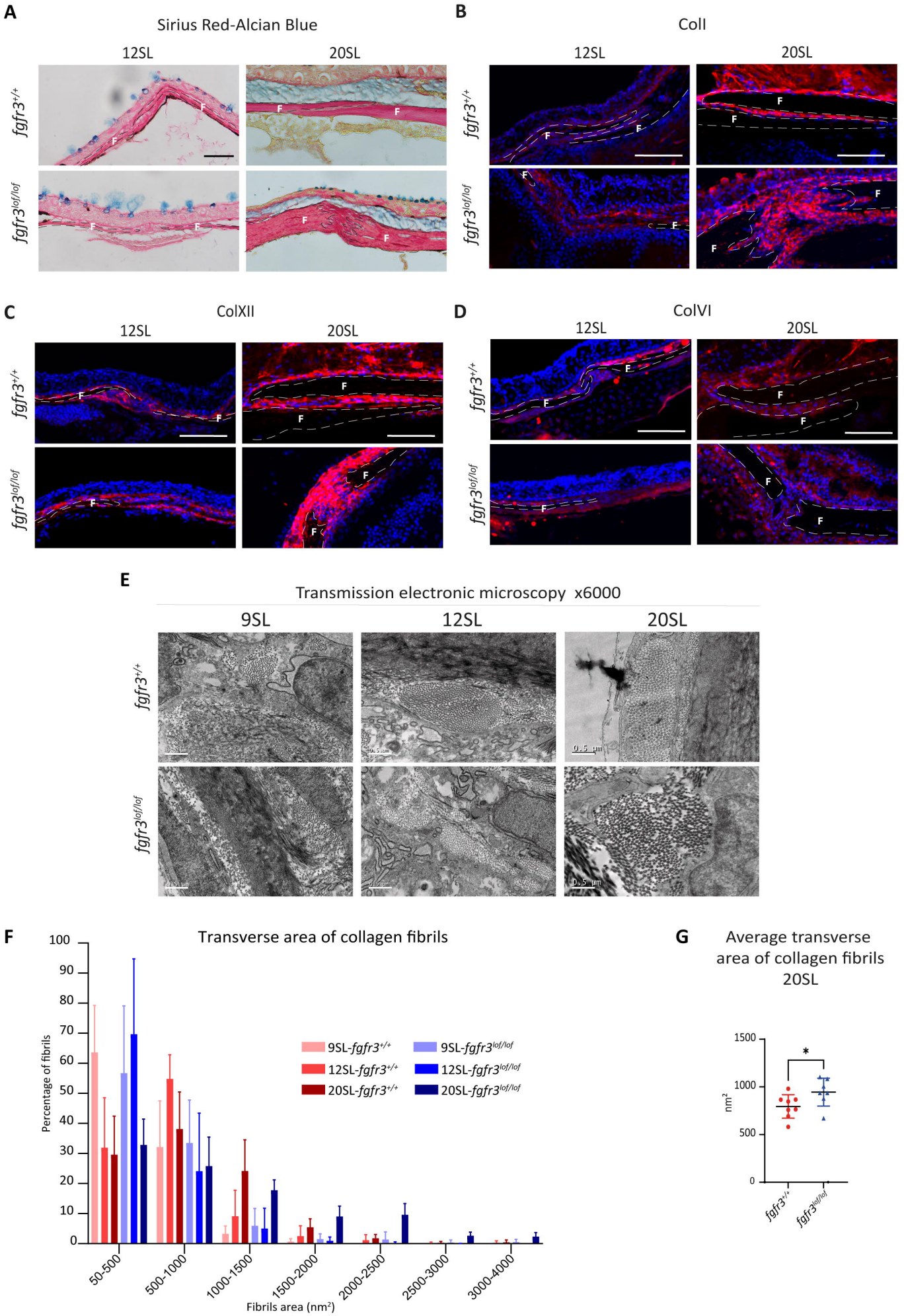
A
Sirius Red-Alcian Blue
12SL
20SL
fgfr3+/+
fgfr3lof/lof
B
Coll
C
ColXII
D
ColVI
E
Transmission electronic microscopy x6000
9SL
0.5 µm
F
Transverse area of collagen fibrils
Percentage of fibrils
Fibrils area (nm²)
50-500
500-1000
1000-1500
1500-2000
2000-2500
2500-3000
3000-4000
9SL-fgfr3+/+
12SL-fgfr3+/+
20SL-fgfr3+/+
9SL-fgfr3lof/lof
12SL-fgfr3lof/lof
20SL-fgfr3lof/lof
G
Average transverse area of collagen fibrils 20SL
nm²
*

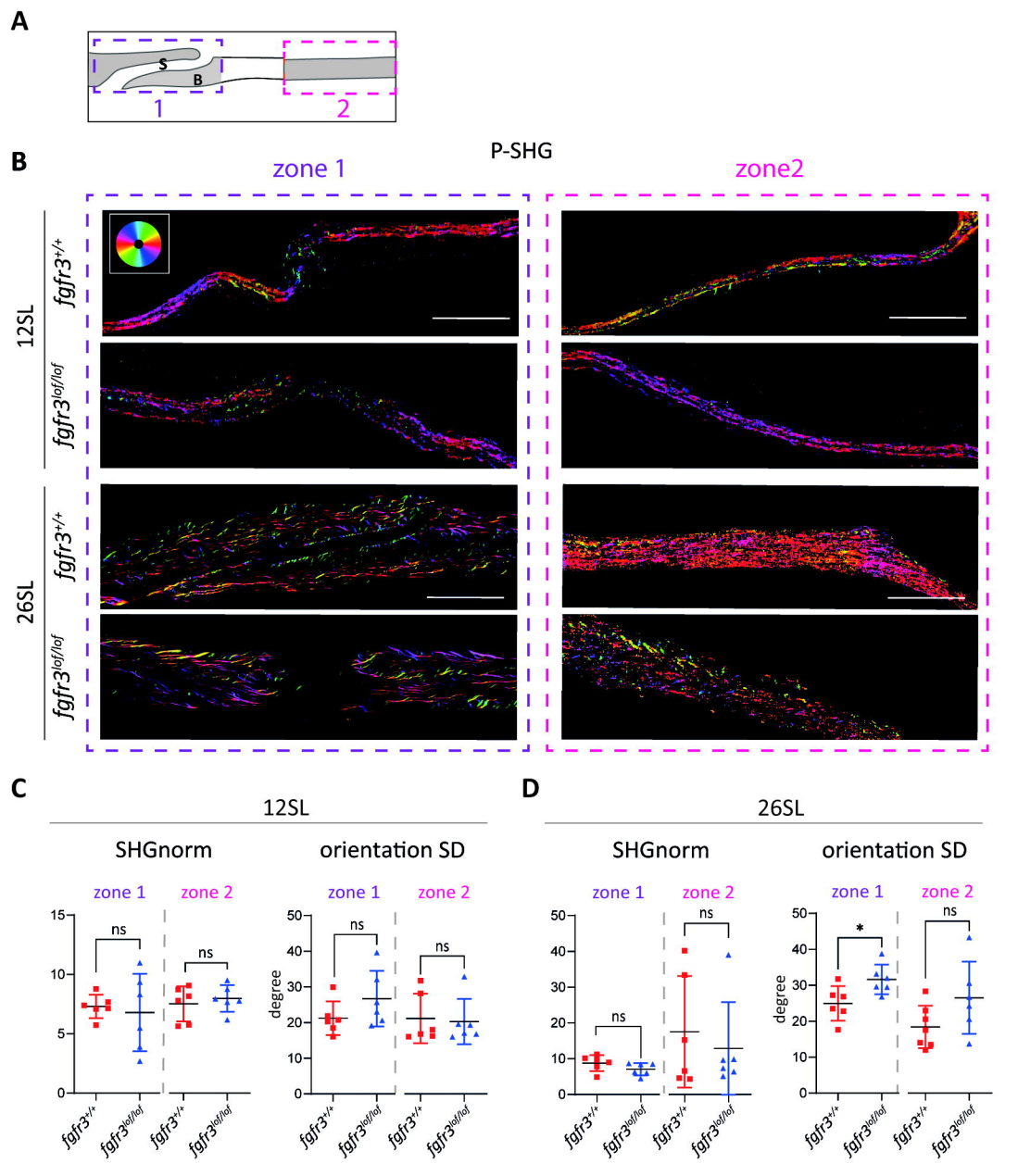
A
S
B
1
2
B
P-SHG
zone 1
zone2
12SL
26SL
fgfr3+/+
fgfr3lof/lof
C
12SL
SHGnorm
orientation SD
zone 1
zone 2
ns
degree
D
26SL
*

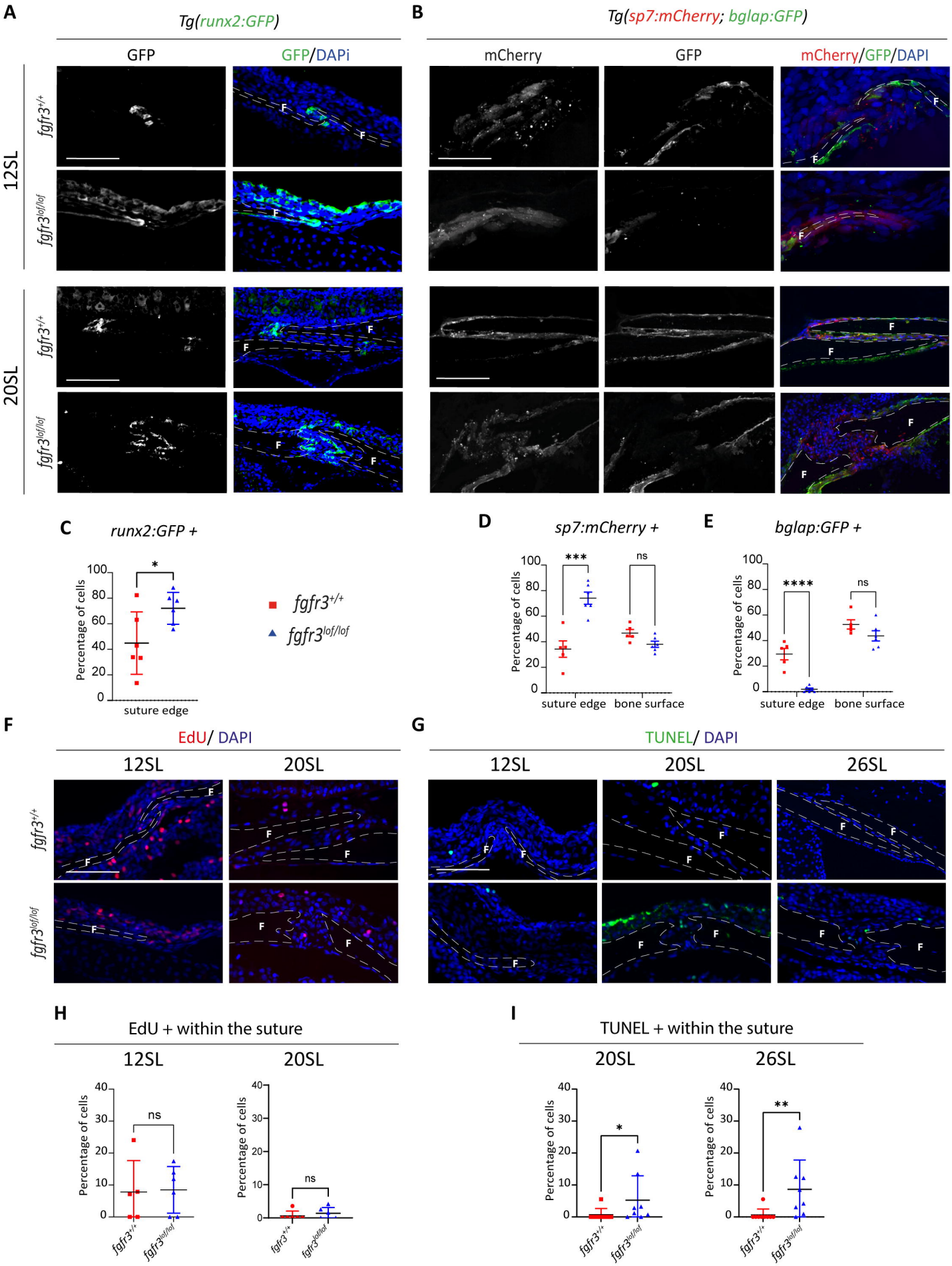
A
Tg(runx2:GFP)
GFP
GFP/DAPi
12SL
20SL
fgfr3+/+
fgfr3lof/lof
F
B
Tg(sp7:mCherry; bglap:GFP)
mCherry
GFP
mCherry/GFP/DAPI
C
runx2:GFP +
Percentage of cells
suture edge
*
fgfr3+/+
fgfr3lof/lof
D
sp7:mCherry +
***
ns
suture edge
bone surface
E
bglap:GFP +
****
ns
suture edge
bone surface
F
EdU/ DAPI
12SL
20SL
G
TUNEL/ DAPI
12SL
20SL
26SL
H
EdU + within the suture
12SL
20SL
ns
ns
I
TUNEL + within the suture
20SL
26SL
*
**

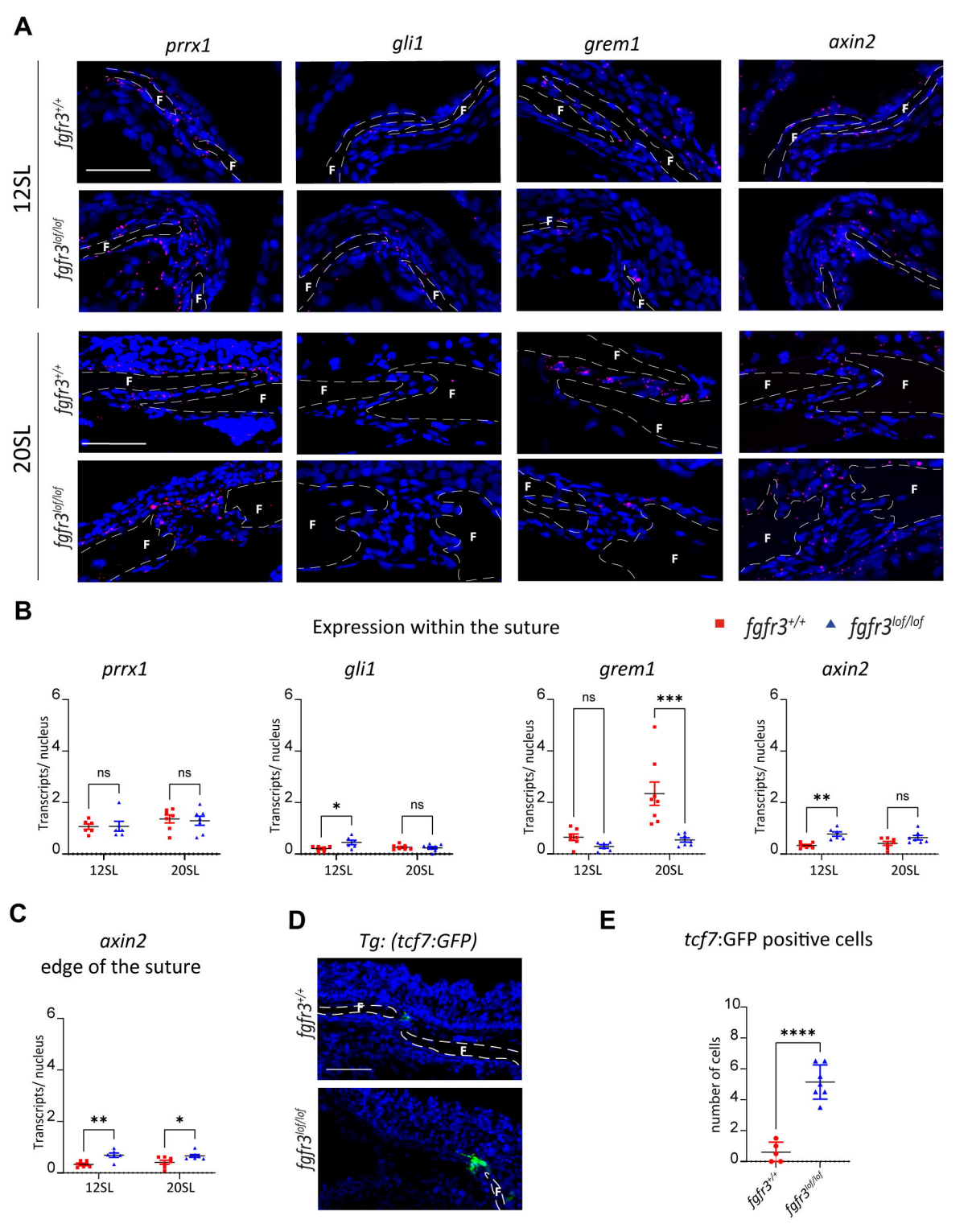
A
prrx1
gli1
grem1
axin2
12SL
20SL
fgfr3+/+
fgfr3lof/lof
F
B
Expression within the suture
fgfr3+/+
fgfr3lof/lof
Transcripts/ nucleus
ns
*
***
**
12SL
20SL
C
axin2
edge of the suture
D
Tg: (tcf7:GFP)
E
tcf7:GFP positive cells
number of cells
****

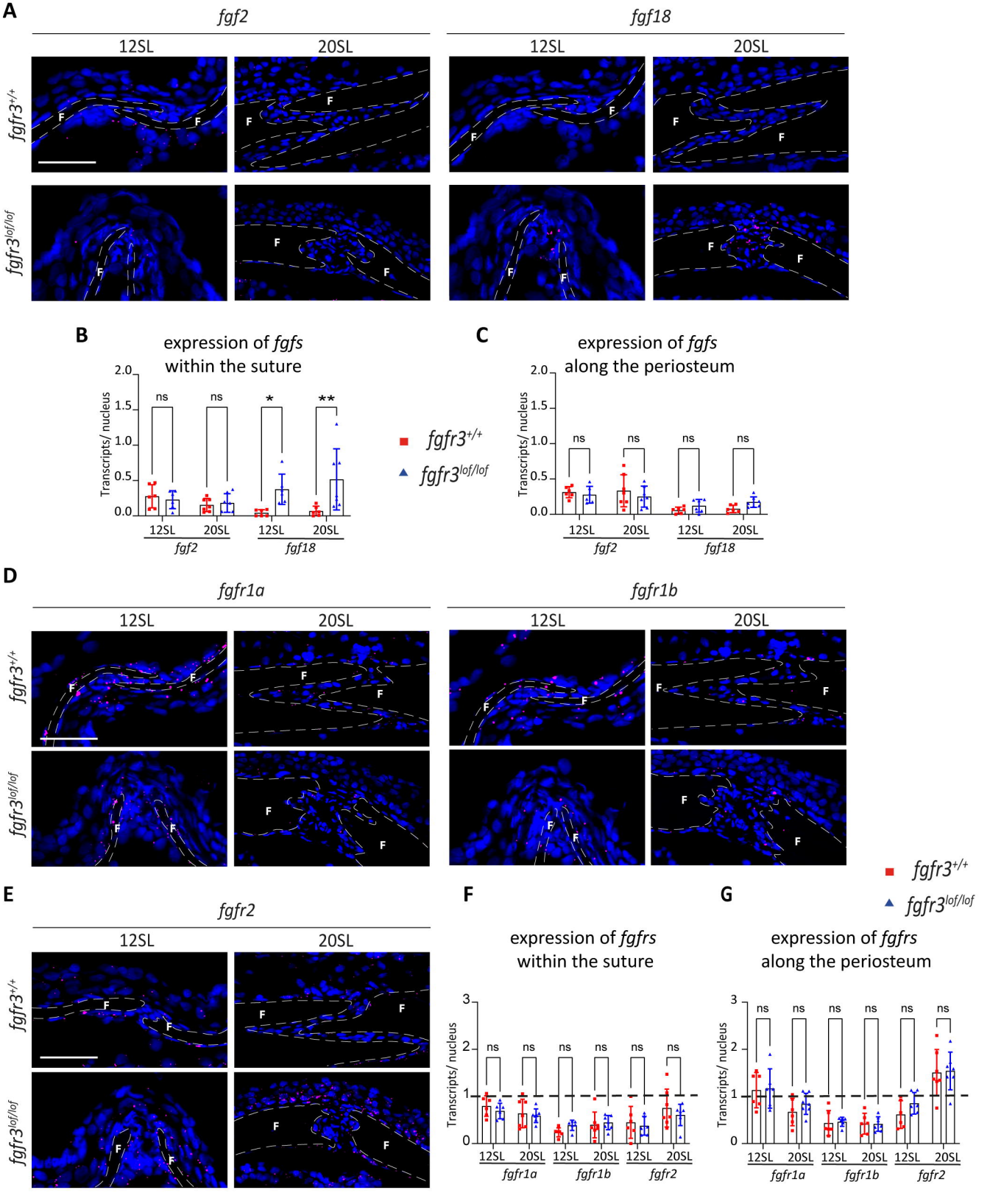
A
fgf2
fgf18
12SL
20SL
fgfr3+/+
fgfr3lof/lof
F
B
expression of fgfs
within the suture
Transcripts/ nucleus
ns
*
**
12SL
20SL
fgf2
fgf18
C
expression of fgfs
along the periosteum
D
fgfr1a
fgfr1b
E
fgfr2
F
expression of fgfrs
within the suture
G
expression of fgfrs
along the periosteum
fgfr1a
fgfr1b
fgfr2

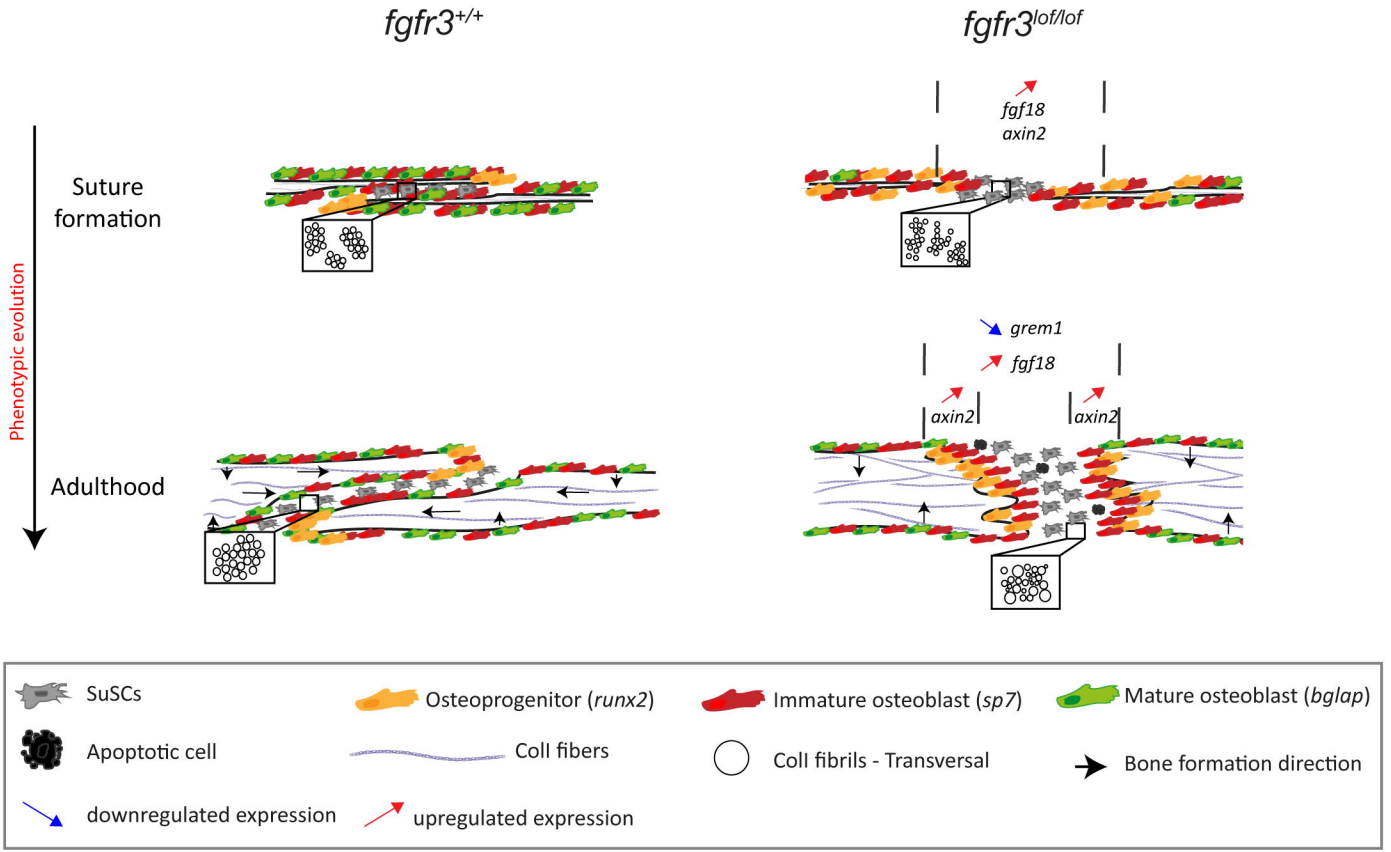
fgfr3+/+
fgfr3lof/lof
Phenotypic evolution
Suture formation
Adulthood
fgf18
axin2
grem1
fgf18
axin2
axin2
SuSCs
Apoptotic cell
downregulated expression
Osteoprogenitor (runx2)
Coll fibers
upregulated expression
Immature osteoblast (sp7)
Coll fibrils - Transversal
Mature osteoblast (bglap)
Bone formation direction